Astronomy & Astrophysics manuscript no. 1614
June 8, 2009

© ESO 2009

arXiv:0906.1533v1 [astro-ph.IM] 8 Jun 2009

Morphological effects on IR band profiles

Experimental spectroscopic analysis with application to observed spectra of oxygen-rich AGB stars

A. Tamanai[1], H. Mutschke[1], J. Blum[2], Th. Posch[3], C. Koike[4], and J.W. Ferguson[5]

[1] Astrophysical Institute and University Observatory, Friedrich-Schiller-University Jena, Schillergäßchen 3, D-07745 Jena, Germany
[2] Institut für Geophysik und Extraterrestrische Physik, Technische Universität Braunschweig, Mendelssohnstr. 3, D-38106 Braunschweig, Germany
[3] Institut für Astronomie, Türkenschanzstrasse 17, A-1180 Wien, Austria
[4] Department of Earth and Space Science, Graduate School of Science, Osaka University, 1-1 Machikaneyama, Toyonaka, Osaka 560-0043, Japan
[5] Department of Physics, Wichita State University, Wichita KS67260-0032, USA

Preprint online version: June 8, 2009

ABSTRACT

Aims. To trace the source of the unique 13, 19.5, and 28 μm emission features in the spectra of oxygen-rich circumstellar shells around AGB stars, we have compared dust extinction spectra obtained by aerosol measurements.
Methods. We have measured the extinction spectra for 19 oxide powder samples of eight different types, such as Ti-compounds (TiO, TiO_2, Ti_2O_3, Ti_3O_5, Al_2TiO_5, $CaTiO_3$), α-, γ-, χ-δ-κ-Al_2O_3, and $MgAl_2O_4$ in the infrared region (10 - 50 μm) paying special attention to the morphological (size, shape, and agglomeration) effects and the differences in crystal structure.
Results. Anatase (TiO_2) particles with rounded edges are the possible 13, 19.5 and 28 μm band carriers as the main contributor in the spectra of AGB stars, and spherically shaped nano-sized spinel and Al_2TiO_5 dust grains are possibly associated with the anatase, enhancing the prominence of the 13 μm feature and providing additional features at 28 μm. The extinction data sets obtained by the aerosol and CsI pellet measurements have been made available for public use at *http://elbe.astro.uni-jena.de*.

Key words. stars:circumstellar matter – stars: AGB and post-AGB – Infrared: stars – methods: laboratory – techniques: spectroscopic

1. Introduction

Dust grains, which are composed mostly of micron-sized solid particles, are crucial players for the initial stages of star and planet formation. A significant dust production source is in the outflow of asymptotic giant branch (AGB) stars which lose almost 90 % of their total mass during mass loss at the end of their life time (e.g. Sedlmayr 1994; Gail & Sedlmayr 1999). Dust formation can only occur if the temperature is low enough and the density of condensable molecules is high enough for condensates to be stable against evaporation. Regions with low temperatures usually occur only at a significant distance above the photosphere with densities that are orders of magnitude lower than in the photosphere of stars (Habing & Olofsson 2004). Notably, observed emission spectra of AGB stars provide information on the physical and chemical properties of dust grains present. Nevertheless, the chemical and mineralogical composition of dust grains in AGB stars are not yet well understood. Depending on temperature and pressure conditions, high temperature condensates (HTCs) such as corundum, spinel and perovskite (e.g. Grossman & Larimer 1974; Sharp & Huebner 1990) are most important because they contribute significant opacity when no other grains are present, even though they are not as abundant as the silicate or iron grains which form at lower temperatures. Once the more abundant grains begin to condense, these less abundant grains lose their significance. Although they are significant only over a narrow range of temperatures, it is an important transition region between the molecular regime and the dust regime (Ferguson et al. 2005).

The strong and unique 13 and 19.5 μm emission features detected from oxygen-rich (O-rich) circumstellar envelopes around evolved stars may conceivably be caused by HTCs.

A crystalline form of Al_2O_3 has been considered as a carrier of the 13 μm feature (e.g. Onaka et al. 1989; Glaccum 1995; Begemann et al. 1997; Sloan et al. 2003; Stroud et al. 2004; DePew et al. 2006). Begemann et al. (1997) demonstrated that amorphous Al_2O_3, which was fabricated by a sol-gel technique, is not able to explain the 13 μm feature of circumstellar O-rich envelopes. However, they suggested that crystalline α-Al_2O_3 may be the 13 μm band carrier if the particle shape is taken into consideration. Silicate dust grains might be closely related to the 13 μm band as well. Sloan et al. (2003) investigated the correlated dust features at 13, 20, and 28 μm of O-rich circumstellar shells and suggested that crystalline Al_2O_3 is the 13 μm feature carrier rather than spinel, and that the 20 and 28 μm features are contributed by silicates. Stroud et al. (2004) also proposed that crystalline corundum seems to be a promising candidate for the 13 μm feature due to the structure and composition of two formes presolar Al_2O_3 grains which were discovered in the Tieschitz ordinary chondrite. These structural and compositional differences are directly linked to the condensation sequence of dust grains and reflect the observed spectra. There is absence of the 22 μm feature from crystalline corundum in observed spectra as well. DePew et al. (2006) studied the IR spectrum features at 13 and 21 μm of AGB stars using the one-dimensional radiative transfer code DUSTY. The target species were corundum, spinel, silicate, and amorphous alumina, and included the effects of grain shape and relative abundances of mixing samples. They found that corundum fit well as the 13 μm feature carrier rather than spinel if the grains have a spherical shape.

However, Posch et al. (1999) have shown that neither corundum nor rutile could account for the 13 μm emission band because the peak position of corundum was located at slightly shorter wavelength (12.7 μm). Only spherical spinel corresponded closely to the 13 μm emission band (12.95 μm) in their theoretical calculations. Fabian et al. (2001) have examined experimentally the spectra of synthesized spinel by taking different Al/Mg-ratios into account. They found out that the peak position of the near-stoichiometric synthetic spinel (e.g. $Mg_{1.01}Al_{1.99}O_4$ and $Mg_{0.94}Al_{2.04}O_4$) fit well at 13 μm compared with the spectra of O-rich circumstellar shells.

Speck et al. (2000), on the other hand, proposed silicon dioxide (SiO_2) or polymerized silicates as a 13 μm feature carrier candidate. They suggested that the 13 μm feature is contributed by the silicates in a similar way to Begemann et al. (1997). Speck et al. (2000) exhibited two polytypes of SiO_2 which produced a comparatively clear 13 μm band and also pointed out that a detectable amount of SiO_2 formation is feasible considering the atomic abundances.

Heterogeneous dust grains have been considered for the identification of the 13 μm feature as well. Kozasa & Sogawa (1997) proposed core-mantle grains which were composed of an α-Al_2O_3 core surrounded by a silicate mantle as a possible candidate for the 13 μm carrier. Posch et al. (1999) examined the 13 μm band profile by making use of the Maxwell-Garnett theory. When the volume fraction of corundum was 0.85 (corundum core 85 % and amorphous olivine mantle 15 %), the peak position in the spectrum was at 12.95 μm in wavelength.

Based upon a model calculation of O-rich circumstellar dust shells around pulsating AGB stars, Jeong et al. (1999) stated that TiO_2 would be the most promising candidate as the nucleation seed for further heterogeneous grain growth instead of Al_2O_3. Until now, the presence of TiO_2 dust grains in spectra of AGB stars has not been confirmed; however, they were identified in meteorites such as carbonaceous chondrites (Greshake et al. 1996, 1998) and the Krymka unequilibrated ordinary chondrites (Nittler et al. 2005). Presolar titanium oxide in unequilibrated ordinary chondrite meteorites has been reported (Nittler et al. 2008). Greshake et al. (1996) suggested that these oxides did not undergo further chemical reactions with remaining nebular gas during the formation of different oxide or silicate dust grains. According to elemental abundances in meteorites (Cameron 1973), magnesium (Mg), silicon (Si), and iron (Fe) are more abundant than aluminum (Al) and calcium (Ca) by a factor of 12. Titanium (Ti) is a much less abundant metal; it is a factor of 400 times less abundant than Si. Thus Mg-, Si-, Fe-, Al-, and Ca-compounds surpass Ti-compounds in quantity.

Experimentally measured spectra and theoretical calculations which assume simple geometrical models such as spherical (Mie 1908) or ellipsoidal (Bohren & Huffman 1983) grain shapes have been generally applied to compare models with observed spectra. It has recently become possible to utilize specific methods for particularly inhomogeneous structures and arbitrarily shaped particles for absorption, scattering and extinction calculations (e.g. Purcell & Pennypacker 1973; Drain 1988; Mishchenko 1990; Mackowski & Mishchenko 1996; Min et al. 2005). However, predictions based on these calculations are uncertain since, in reality, grain shape might be tremendously irregular and complex.

Regarding experimental approaches, absorption spectra have been measured by the KBr (potassium bromide) pellet technique for the mid-IR region in most cases (e.g. Dorschner et al. 1978; Koike et al. 1981; Orofino et al. 1991; Posch et al. 1999; Chihara et al. 2002). A controversial point of this technique is that the band profile is substantially changed by the influence of its electromagnetic polarization since a solid sample is embedded in a medium (KBr) (Fabian et al. 2001).

In this paper, we have experimentally investigated the extinction spectra of α-, γ-, χ-δ-κ-Al_2O_3, $MgAl_2O_4$, and Ti-compounds (TiO, TiO_2, Ti_2O_3, Ti_3O_5, Al_2TiO_5, $CaTiO_3$) in the mid-IR region (10-50 μm) to clarify the possible 13, 19.5 and 28 μm band carriers with special consideration of morphological effects by the use of the aerosol technique (e.g. Hinds 1999) so as to avoid the influence of electromagnetic interaction with solid embedding media (Tamanai et al. 2006a,b). The aim is to obtain band profiles without the medium effect of these HTCs for a direct comparison to observed spectra and to identify the possible candidates.

2. Experiment

2.1. Classical vs. aerosol techniques

The pellet technique is the classic technique, where a solid sample is mixed with potassium bromide (KBr), cesium iodide (CsI), or polyethylene (PE) powder that have high transmission through certain IR wavelength ranges, and the mixture is pressed with a 10 Ton load in order to make a 0.55 mm thick (1.2 mm for PE) and 13 mm diameter pellet for spectroscopic analysis (e.g. Koike & Hasegawa 1987; Jäger et al. 1994; Begemann et al. 1997; Chihara et al. 2002). The advantages of the pellet technique are low cost, low sample consumption, longevity of the pellets in a desiccator and the exact amount of a measured sample is known. On the other hand, the main disadvantage is that there is the possibility of environmental effects due to the electromagnetic polarization of the embedding medium (e.g. Papoular et al. 1998; Henning & Mutschke 2000; Speck et al. 2000; Clément et al. 2003). Tamanai et al. (2006a,b) introduced the aerosol technique into dust grain investigation and demonstrated that the strong absorption peaks at approximately 9.8 and 11 μm obtained by aerosol measurements for an olivine-type crystalline powder are shifted to shorter wavelengths by amounts of up to 0.24 μm compared with spectra obtained by the KBr pellet measurements. Conversely, weak features are not affected much by the KBr medium effect (see more details in Tamanai et al. 2006b).

Fig. 1 shows the setup of the apparatus for the aerosol measurement. We have utilized a dust flow generator (Palas RBG1000) to disperse a powdered sample in a nitrogen (N_2) gas stream. The dense aerosol is carried to a two-stage impactor which separates the large particles from the small ones ($d_{avg} \approx$ 2-3 μm). The small-grained aerosol are concentrated by the impactor so that a concentration of 10^6 particles per cubic centimeter finally arrives at a White-type long-path infrared cell (MARS-8L/20V, Gemini Scientific Instr.) which has an 18 m path length by taking advantage of multiple reflections between two gold mirrors mounted on both sides in order to increase the sensitivity. Since a Fourier Transformation Infrared Spectrometer (FTIR, Bruker 113v) with a DTGS detector with CsI windows is fixed to the cell, it is possible to measure the extinction spectrum of the suspended dust particles in N_2 gas. As a consequence, we avoid any environmental effect during the aerosol measurement, and the measurement conditions are closer

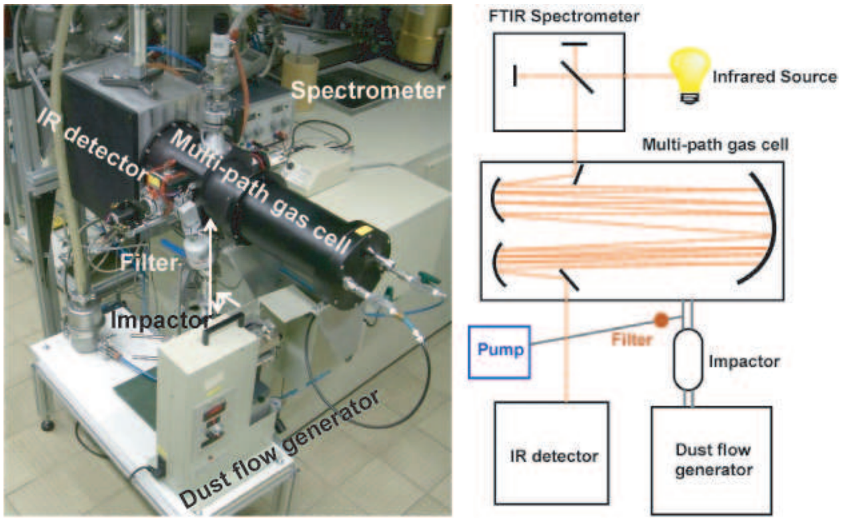

Fig. 1. Experimental apparatus for aerosol extinction measurements. A photo (left) and a schematic diagram (right) of experimental device setup.

to a vacuum with regard to the dielectric function of the medium (N_2: $\epsilon\approx1.0$) compared to KBr (ϵ=2.3). Moreover there is a risk of deforming the powdered sample structure by the high pressure required for the KBr pellet technique, which is avoided when the aerosol technique is utilized for the measurement.

To make the environmental effect clearer, we have used CsI powder to create pellets as well. CsI is particularly transparent between 2 and 50 μm wavelengths, and has a greater optical constant than that of KBr (CsI 1.74 & KBr 1.52). We have extended the wavelength range up to 50 μm for both aerosol and CsI pellet measurements. The aerosol particles are extracted on a polyester-membrane filter which is mounted externally between the outlet of the impactor and the cell. The morphological properties of extracted particles are investigated with a scanning electron microscope (SEM).

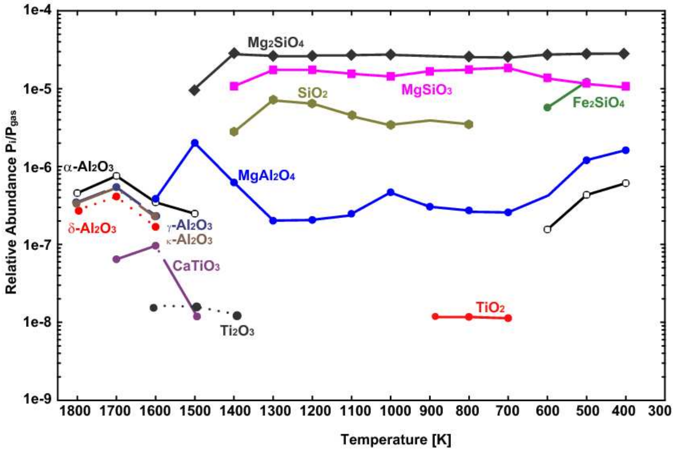

Fig. 2. Relative abundances of dust grain species for a single gas pressure (10^4 dyne/cm^2) as a function of temperature.

2.2. Samples

We have investigated 19 powdered crystalline samples of eight different combinations of composition and crystal structure. In particular, for TiO_2 and Al_2O_3, special attention is paid to the difference in the crystal structures, and $MgAl_2O_4$ and TiO_2 are utilized for morphological examination. Table 1 gives a list of the investigated samples including their properties. All the samples are commercial products. Since our aerosol apparatus is highly effective only for particle sizes of less than about 1 μm, Al_2TiO_5 (original size $\approx$ 149 μm) and Ti_3O_5 (original size 0.1-0.3 mm) were milled by a ball mill process (Si_3N_4 balls for 30 min.) to obtain particle sizes less than 1 μm. In addition, a size fraction $<$ 1 μm in diameter for χ-δ-κ-Al_2O_3 is concentrated by sedimentation in a solvent (acetone).

Detailed information of each oxide is given in Appendix A.

2.3. Equation of state

The equation of state (EOS) of the PHOENIX stellar atmosphere code can calculate the chemical equilibrium (gas and dust in equilibrium) of 40 elements, including the ionization stages, with hundreds of molecular, liquid, and solid species (see details in Allard et al. 2001; Ferguson et al. 2005). Although the EOS does not provide information on the chemical pathways, it is possible to obtain number fractions of dust species at specific temperature and pressure points. We use the PHOENIX EOS for our spectroscopic investigation since it can predict the abundance patterns of various dust species in the outflow of AGB stars. Fig. 2 shows the abundances of condensates as a function of temperature for a single gas pressure, 10^4 dyne/cm^2. The first dust species to condense are four different crystal structures of Al_2O_3 at approximately 1800 K. The most abundant one is α-Al_2O_3 followed by γ-, κ-, δ-Al_2O_3. Then, perovskite appears at around 1700 K. Solid Ti-compounds such as Ti_2O_3 and TiO_2 come out of the gas phase below 1600 K. TiO_2 appears below 1000 K. However, Ti-compounds are less abundant than silicates by a factor of 1000 because Ti is a factor of 400 less abundant metal than Si (Cameron 1973). The most abundant species above 1500 K is spinel which appears at about 1600 K in this calculation. Mg-rich silicate grains dominate below 1500 K (Note: We plotted only 12 species that have been investigated in our experiments here).

We concentrate on those HTCs (Al_2O_3, spinel, and Ti-

Table 1. Properties of the samples

Chem. formula	Mineralogical name	Product Info.	Abbr.	Size (μm)	Shape	Sect.
TiO	Titanium monoxide	Aldrich	TiO	0.1-2.0	irr. w/ sharp edges	A.1.
α-TiO_2	Rutile	Aldrich	CR1	0.1-0.5	irr. w/ round. edges	A.2.
α-TiO_2	Rutile	Alfa Aesar	CR2	0.1-0.5	irr. w/ sharp & round. edges	A.2.
α-TiO_2	Rutile	Tayca 150W	CR3	0.01-0.08	thin & long	A.2.
α-TiO_2	Rutile	Chitan Inc. No.101	CR4	0.01-0.1	sph. & ellip.	A.2.
β-TiO_2	Anatase	Alfa Aesar	CA1	0.1-0.6	round. edges	A.2.
β-TiO_2	Anatase	C.P.	CA2	0.1-0.2	round. & squ. & ellip.	A.2.
β-TiO_2	Anatase	Tayca 600	CA3	0.01-0.05	round.	A.2.
β-TiO_2	Anatase	Chitan Inc. No.9	CA4	$\approx$ 0.05	round. & long-narrow	A.2.
Ti_2O_3	Dititanium trioxide	Alfa Aesar	Ti_2O_3	0.2-1.5	irr. w/ sharp edges	A.3.
Ti_3O_5	Trititanium pentoxide	Alfa Aesar	Ti_3O_5	0.1-1.0	irr. w/ sharp edges	A.4.
$CaTiO_3$	Perovskite	Alfa Aesar	$CaTiO_3$	0.03-0.5	irr. w/ sharp edges	A.5.
Al_2TiO_5	Tialite	Alfa Aesar	Al_2TiO_5	0.05-0.6	irr. w/ very sharp edges	A.6.
α-Al_2O_3	Corundum	Alfa Aesar	CAC1	0.3-0.5	irr. w/ round. edges	A.7.
α-Al_2O_3	Corundum	Glaschemie Jena	CAC2	0.06-1.0	irr. w/ sharp edges	A.7.
γ-Al_2O_3		Alfa Aesar	CG	0.1-0.3	squ. w/ round. edges	A.7.
χ-δ-κ-Al_2O_3		C.P.	CCDK	0.05-1.0	irr. & tabular	A.7.
$MgAl_2O_4$	Spinel	Alfa Aesar	CSp1	0.04-0.5	irr. w/ sharp & round. edges	A.8.
$MgAl_2O_4$	Spinel	Aldrich	CSp2	$\approx$ 0.05	sph.	A.8.

"C.P." → commercial product; "irr." → irregular; "round." → roundish; "squ." → square; "ellip." → ellipsoidal; "sph." → spherical

compounds) for experimental spectroscopic analysis (Note: We call HTCs in this paper those species for which dust grains condense out of the gas phase above 1500 K in this EOS calculation, plus TiO_2).

3. Spectroscopic results

3.1. Aerosol versus CsI pellet spectra

The aerosol spectra reveal substantially different band profiles in comparison with the CsI pellet measurements. Tamanai et al. (2006b) demonstrated the disparity between aerosol and KBr pellet spectra of various silicate samples. Fig. 3 shows the three extinction spectra of rutile (CR1) up to 25 μm obtained by aerosol, CsI, and KBr pellet measurements. The strongest peak at 13.53 μm of the aerosol spectrum shifts to 15.61 μm in wavelength with the CsI pellet measurement ($\Delta\lambda$=2.08 μm). The shift is larger than in the case of the KBr spectrum which is explained by the relationship between the dielectric functions of a sample (ϵ) and the embedding medium (ϵ_m) (see Bohren & Huffman 1983). As the value of ϵ_m increases (N_2 1.0; KBr 2.3; CsI 3.0), the peak positions are significantly shifted to longer wavelengths by the influence of its electromagnetic polarization.

Fig. 4 shows the extinction spectra in the wavelength range between 10 and 50 μm for all 19 samples which are plotted as normalized extinction (except TiO). The extinction spectra are normalized because aerosol measurements are not quantitative. TiO has a featureless spectrum in both the aerosol and CsI measurements because it is dominated by free charge carrier absorption. The rutile spectra are characterized by a strong, often double-peaked, absorption band between 12 and 22 μm (as already shown in Fig. 3), a second absorption band between 22 and 27 μm, and a third very broad one between 27 and 50 μm, which is much more centered at the short-wavelength side for the CsI spectra. For one sample (CR3), these three bands are merged into a very broad complex. The strong difference between these spectra and those calculated by Posch et al. (1999) and Posch et al. (2003) for spherical grains will be discussed in the next Section. Compared to rutile (TiO_2), anatase (TiO_2) lacks the second of the bands and the first one instead extends to somewhat longer wavelengths ($\approx$ 27 μm). Also, the 12-27 μm band in two cases (CA3 & CA4) shows strongly pronounced differences between the aerosol and the CsI spectra. While in the first case it is double-peaked, in the second it has only a single-peaked profile with the peak at 16-18 μm. On the other hand, the long-wavelength band has not been observed to be so strongly broadened beyond 40 μm as seen for the rutile samples CR1 and CR4.

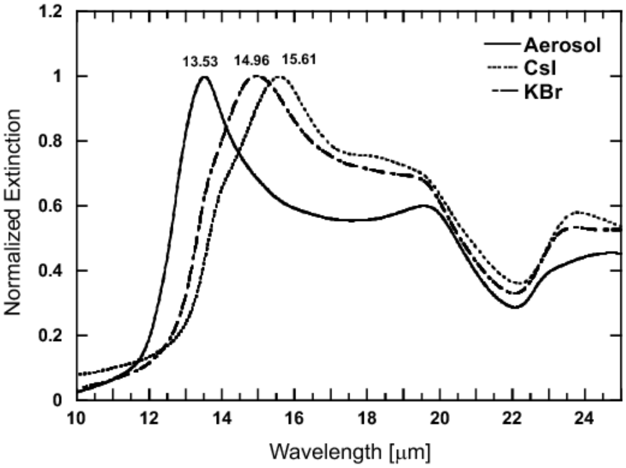

Fig. 3. Normalized extinction vs. wavelength of TiO_2 (CR1) spectra obtained by aerosol (solid line), CsI (dotted line), and KBr pellet measurements (dash-dotted line).

The calculations for spherical particles presented by Posch et al. (2003) produce a double band peaking at 13 and 15 μm and a sharp 27.5 μm band. The CA1 and CA2 aerosol spectra come relatively close to this prediction, although the profiles are much broader (see next section). Ti_2O_3 has a double-peaked band between 17 and 21 μm and only weak features longward of it. The aerosol-measured spectrum reproduces very well the calculated spectrum for spherical particles (Posch et al. 2003).

The (normalized) spectrum of CsI embedded particles shows an enhanced far-infrared extinction, which is probably due to conductivity and certainly is enhanced by agglomeration within the pellet (see also the TiO spectrum). The Ti_3O_5 spectrum does not show this effect, but is complicated in terms of the appearance of many peaks. These peaks do not group into clear complexes, unlike the simpler titanium oxides.

Perovskite again has a divided spectrum with a relatively narrow short-wavelength band, the peak of which shifts strongly with the embedding medium. Even for the aerosol spectrum, the peak is at longer wavelengths compared to the calculated spectrum for spherical grains presented by Posch et al. (2003), whereas the longer-wavelength bands reproduce the calculated band positions quite well. The aluminum titanate spectrum lacks this division and is in fact reminiscent of the γ-Al_2O_3 spectrum with some additional smaller structures, but not as many as the χ-δ-κ-Al_2O_3.

Koike et al. (1995) performed extinction efficiency measurements of two different γ-Al_2O_3 samples (commercial aerosil particles and a combustion product). Both samples showed a double peak at approximately 12.4 and 13.9 μm. Similarly, Kurumada et al. (2005) carried out transmittance measurements of commercial γ-Al_2O_3 particles, and they detected a double peak at about 12.5 and 13.5 μm in wavelengths as well. These results fit well with our measurements (aerosol 12.3-13.1 μm & CsI 12.7-13.6 μm). Moreover, the aerosil spectrum from Koike et al. (1995) exhibited also a small shoulder around 17-18 μm. The small shoulder is apparent in our γ-Al_2O_3 spectra obtained by both the aerosol (15.7 μm) and CsI pellet (16.6 μm) measurements. The slight differences in peak positions come from mainly two factors. One is the medium effect since all observations utilized different substances as a medium. Koike et al. (1995) and Kurumada et al. (2005) used KBr powder whereas we applied N_2 gas for the aerosol measurements and CsI for the pellet measurements. Another factor is the morphological effect. Our γ-Al_2O_3 particles are square shape with rounded edges and 0.1-0.3 μm in size while the aerosil particles (Koike et al. 1995) were disk shape with a mean diameter of 0.02 μm.

Corundum shows two strong band complexes at 11-18 and 19-23 μm plus a small band at 26 μm. Both complexes have clear substructures, although the structure strongly depends on the sample (see below). The spectra do not show dominant sharp peaks at 13 μm or shortward of 13 μm, which would be expected for spherical grains according to Mie calculations (Begemann et al. 1997; Posch et al. 1999).

Another important point for Al_2O_3 is the state of its crystal structure. Though it is obvious to confirm the morphological differences among these Al_2O_3 samples via the SEM and TEM images, these band profiles are significantly affected by differences in the crystal structures, in this case more than by the morphological effects.

Kurumada et al. (2005) produced nano-sized spherical δ-Al_2O_3 particles by the gas evaporation method and measured the transmittance spectra by making use of the KBr pellet technique. They detected 15 absorption peaks in the wavelength range between 10 and 19 μm. δ-Al_2O_3 showed many sharp peaks in an exceptionally broad absorption region (10-20 μm). A similar result is obtained in our χ-δ-κ-Al_2O_3 sample investigation up to 20 μm, and more peaks are observed in both the aerosol and CsI pellet spectra up to 46 μm.

The relation between cubic alumina and (non-stoichiometric) spinel spectra has already been discussed by Fabian et al. (2001) based on reflection spectra. It is interesting to note that the aerosol measurement of γ-alumina shows a dominance of the 12.5 μm peak in the spectrum and a shift of this feature to shorter wavelengths compared to the CsI measurement. The spectrum comes rather close to that calculated by Begemann et al. (1997) for a shape distribution from the optical constants presented by Koike et al. (1995), although an additional shoulder at 15.7 μm is seen. This shoulder becomes a strong band in the CsI spectrum.

The spinel spectra show two main bands at about 13-14 μm and 17-19 μm depending on sample and embedding. The band at 32 μm is also clearly seen in both the aerosol and CsI spectra. Based on calculations for spherical grain shapes, Fabian et al. (2001) proposed that synthetic and also annealed natural spinel particles would reproduce the 13 μm band of AGB stars. Our samples CSp1 and CSp2 both are synthetic material. The CSp2 spectrum measured in aerosol peaks at 13.26 μm, but when measured in CsI, the peak is shifted to more than 14 μm, which is similar to the position reported by Posch et al. (1999) for spinel particles in KBr. The CSp1 spectra peak at more than 14 μm in all cases, which will be discussed in the next section.

In general, there is a clear trend that the aerosol spectra have peaks at significantly shorter wavelengths than the CsI spectra. In particular, this is always true for the shortest-wavelength peak. However, as already mentioned for anatase, in most cases the matrix effect cannot be reduced to a simple peak shift. Specifically for strong bands, the band profiles measured in aerosol sometimes show a broadening to longer wavelengths as well, sometimes resulting in a secondary peak and a near-rectangular total profile. These effects are seen to a much lesser extent in the CsI spectra. This may partially also be a consequence of differences in the particle morphology, which may have been caused by
(a) using different dispersion methods;
(b) particles may transform during the grinding procedure;
(c) powdered sample structure deformation caused by the high pressurization required for the CsI pellet technique.
A large difference in band profiles between the aerosol and CsI pellet measurements is possibly produced more by spherical and ellipsoidal shapes than irregular ones.

3.2. Morphological effects

One of the advantages of using the aerosol technique in the investigation of dust is that it is possible to inspect the particle morphology. We set a polyester-membrane filter between the outlet of the impactor and the cell (Fig. 1) and extract the incoming aerosol particles. These captured aerosol particles are analyzed by a SEM. The SEM images are shown in Fig. 4 (right). A TEM has also been utilized to understand the individual particle shape as well (Fig. 4 middle images).

The spectrum of CR1 (Fig. 4(b)) shows a similar band profile to that of CR4 in Fig. 4(e). Although the particle sizes of these samples are different from each other, there are two major similarities. The individual particle shape is irregular with roundish edges. The agglomerate state is composed of many elongated and porous agglomerates. It is a characteristic of aerosol particles that chainlike agglomerates are formed by charged particles (Hinds 1999). While the individual particle size of the CR4 sample is smaller than that of CR1, the agglomerate size of CR4 is much larger than that of CR1. As the particle size decreases, it becomes more difficult to remove particles from surfaces when the relationship between adhesive and separating forces are taken into account (Hinds 1999). Differences in the extinction band profile in the region 13-19 μm may be especially influenced by the agglomerate state. Increasing the agglomerate

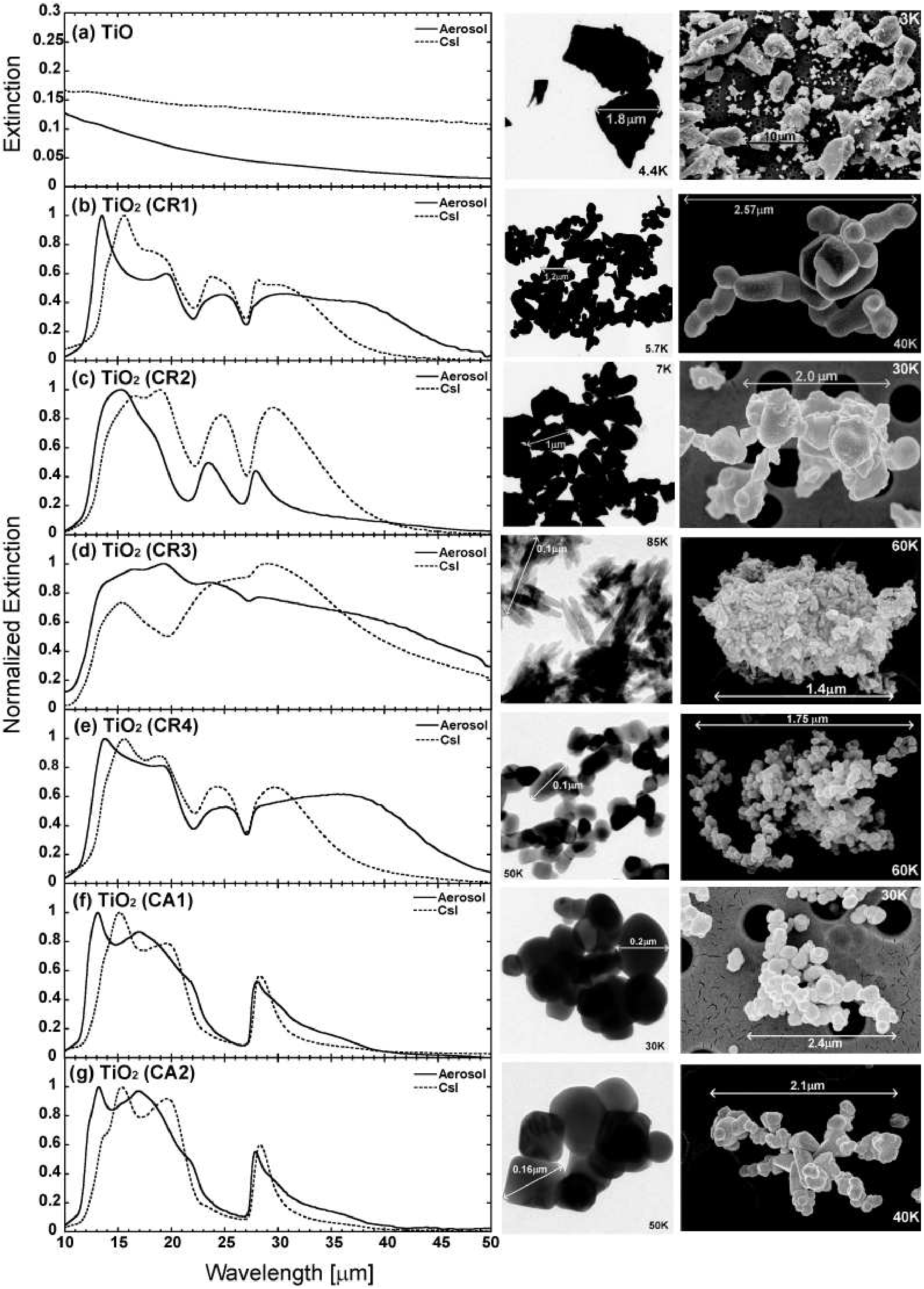

Fig. 4. Left: Normalized extinction vs. wavelength of (a) TiO; (b) TiO_2 (CR1); (c) TiO_2 (CR2); (d) TiO_2 (CR3); (e) TiO_2 (CR4); (f) TiO_2 (CA1); (g) TiO_2 (CA2) spectra obtained by aerosol and CsI pellet measurements. Center: TEM images (original powder). Right: SEM images (aerosol particles). Note that only the TiO spectrum is not normalized.

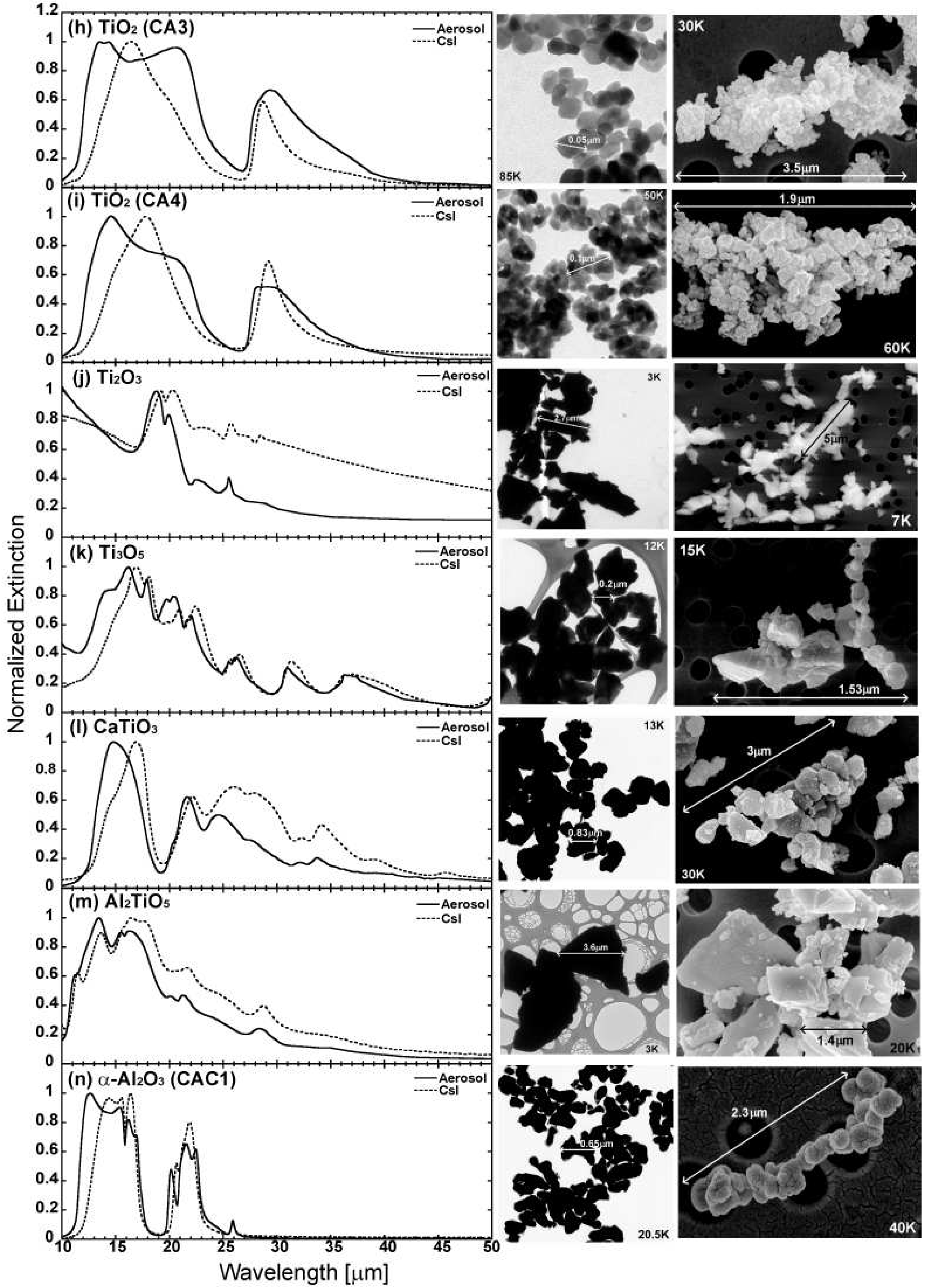

Fig. 4. (*continued*) Left: Normalized extinction vs. wavelength of (h) TiO_2 (CA3); (i) TiO_2 (CA4); (j) Ti_2O_3; (k) Ti_3O_5; (l) $CaTiO_3$; (m) Al_2TiO_5; (n) α-Al_2O_3 (CAC1) spectra obtained by aerosol and CsI pellet measurements. Center: TEM images (original powder). Right: SEM images (aerosol particles).

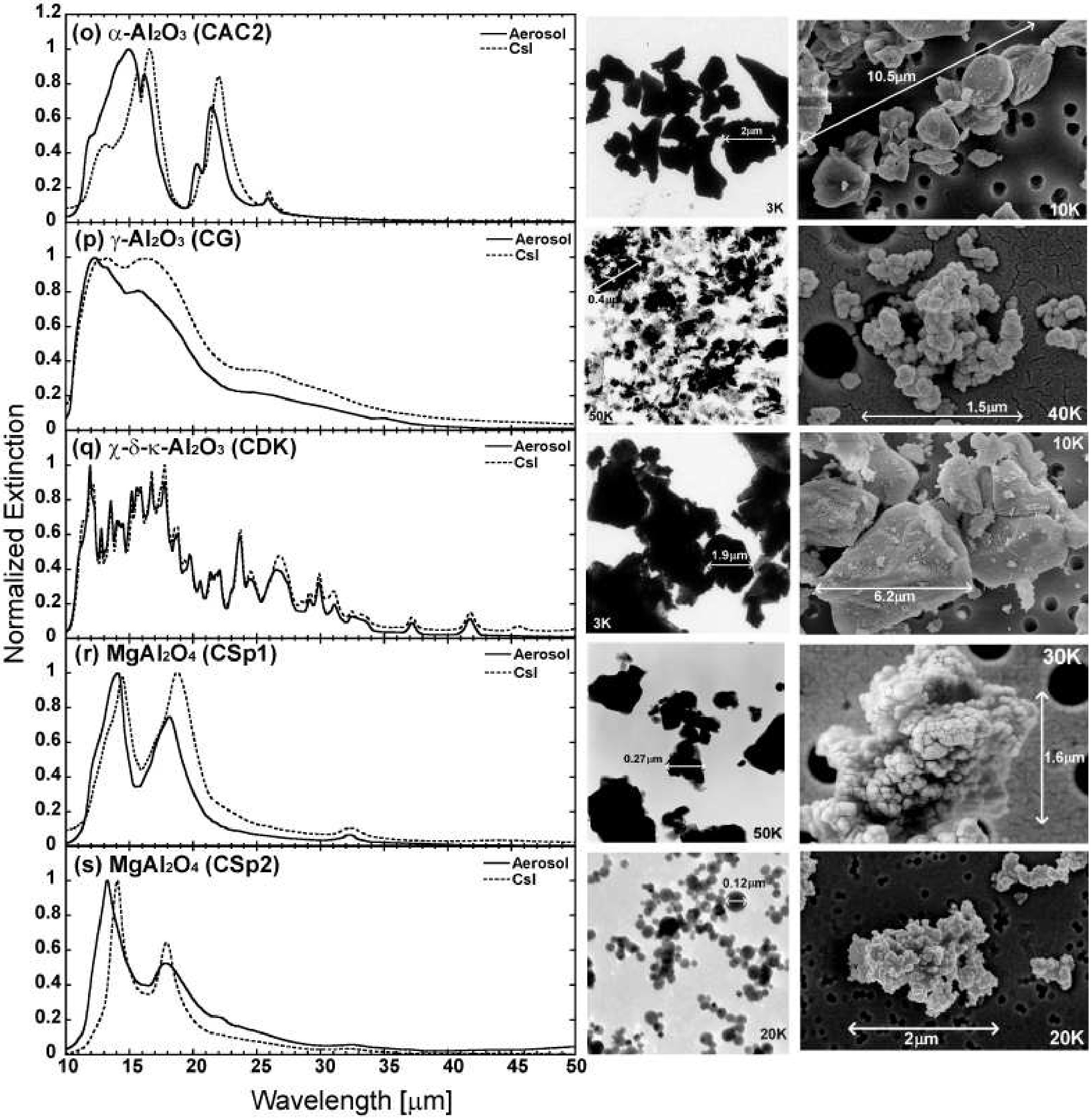

Fig. 4. (*continued*) Left: Normalized extinction vs. wavelength of (o) α-Al_2O_3 (CAC2); (p) γ-Al_2O_3 (CG); (q) χ-δ-κ-Al_2O_3 (CCDK); (r) $MgAl_2O_4$ (CSp1); (s) $MgAl_2O_4$ (CSp2) spectra obtained by aerosol and CsI pellet measurements. Center: TEM images (original powder). Right: SEM images (aerosol particles).

size may cause the broadening of the band in this region towards longer wavelengths. As a result, a sharp fall at 13 μm cannot be seen in the spectrum of CR4. In other words, the secondary peaks at 19 μm increase markedly.

Comparing CR1 and CR2 (Fig. 4(c)), the individual particle sizes are nearly the same, but not the shape. As in the case of forsterite (Tamanai et al. in prep.), irregularly shaped particles (not round edge ones) have a tendency to produce a relatively distinctive single peak at a somewhat longer wavelength. The secondary peak at 19 μm is not seen in the aerosol spectrum of CR2.

Unlike CR1, CR2, and CR4, CR3 (Fig. 4(d)) does not show any clear peaks between 10 and 50 μm in wavelength. The secondary peak at 19 μm seems to dominate. When the agglomerate state is close-packed, a broader band profile can be produced and hide the peaks from view. It is possible to confirm this trend via theoretical calculations as well (Tamanai et al. 2006a).

The theoretical models in the Rayleigh limit of a continuous distribution of ellipsoids (CDE) (Bohren & Huffman 1983) and of spherical particles have been utilized to estimate the magnitude of the extinction profiles for the rutile samples (CR2 & CR4). Two CDE methods have been applied to verify the shape effect on spectra. The CDE2 calculates the extinction efficiency of the most likely near-spherical particle shapes whereas the CDE1 assumes all ellipsoidal shapes with equal probability (see more details in Ossenkopf et al. 1992; Fabian et al. 2001).

Fig. 5 shows the spectra taken from the aerosol measurements (CR2 & CR4) together with the CDE1, CDE2, and Rayleigh calculations. The diameter of the model particles is 0.2 μm and the optical constants from Ribarsky (1985) are ap-

Table 2. The peak positions (μm) for the aerosol and CsI measurements for all samples except TiO.

Chemical formula	Abbrev.	Measurement				Peaks	[μm]			
TiO_2	CR1	Aerosol	**13.53**	**19.56**	**24.70**	**30.30**	**35.80**			
		CsI	15.61	23.77	28.13	29.81				
TiO_2	CR2	Aerosol	**15.33**	**23.50**	**27.95**					
		CsI	16.58	18.94	24.71	29.55				
TiO_2	CR3	Aerosol	**16.47**	**19.25**	**23.39**	**28.27**				
		CsI	15.38	29.01						
TiO_2	CR4	Aerosol	**13.79**	**19.27**	**25.59**	**35.64**				
		CsI	15.51	19.03	24.26	29.68				
TiO_2	CA1	Aerosol	**13.10**	**16.90**	**28.19**					
		CsI	15.20	19.60	28.26					
TiO_2	CA2	Aerosol	**13.22**	**16.90**	**27.90**					
		CsI	15.34	19.56	28.30					
TiO_2	CA3	Aerosol	**13.46**	**14.34**	**20.63**	**29.37**				
		CsI	16.45	28.79						
TiO_2	CA4	Aerosol	**14.58**	**19.89**	**28.26**					
		CsI	17.78	29.19						
Ti_2O_3	Ti_2O_3	Aerosol	**18.22**	**19.90**	**22.62**	**25.54**				
		CsI	19.28	20.30	23.11	25.72	28.53			
Ti_3O_5	Ti_3O_5	Aerosol	**16.21**	**17.91**	**19.73**	**20.36**	**21.69**	**22.07**	**25.44**	**26.06**
			30.89	**35.92**						
		CsI	16.89	18.14	19.87	20.93	24.44	25.64	26.57	31.37
			37.14							
$CaTiO_3$	$CaTiO_3$	Aerosol	**14.85**	**21.67**	**24.56**	**32.13**	**33.71**			
		CsI	16.89	22.18	25.95	27.86	32.30	34.16	38.96	45.70
Al_2TiO_5	Al_2TiO_5	Aerosol	**13.48**	**15.48**	**16.31**	**19.96**	**21.33**	**28.38**		
		CsI	9.56	11.48	13.59	16.54	20.67	21.61	28.72	
α-Al_2O_3	CAC1	Aerosol	**12.65**	**15.37**	**16.16**	**16.91**	**20.14**	**21.57**	**22.48**	**25.92**
		CsI	14.31	14.46	16.39	20.67	21.91	25.91		
α-Al_2O_3	CAC2	Aerosol	**14.92**	**16.16**	**20.30**	**21.45**	**25.89**			
		CsI	13.15	15.63	16.59	20.88	22.01	25.95		
γ-Al_2O_3	CG	Aerosol	**12.32**	**13.13**	**15.71**					
		CsI	12.69	13.60	16.02	24.06				
χ-δ-κ-Al_2O_3	CDK	Aerosol	**11.93**	**12.79**	**13.56**	**14.08**	**14.47**	**15.19**	**15.87**	**16.76**
			17.74	**18.77**	**19.32**	**19.77**	**20.56**	**21.38**	**22.07**	**23.69**
			24.48	**26.62**	**29.15**	**29.89**	**31.09**	**32.46**	**37.20**	**41.70**
		CsI	11.45	11.93	12.19	12.81	13.57	14.07	14.26	14.52
			15.21	15.62	15.88	16.76	17.78	18.58	19.29	19.78
			20.58	21.42	21.78	22.09	23.69	24.53	26.80	28.53
			29.15	29.90	31.06	32.48	33.19	37.18	41.75	45.53
$MgAl_2O_4$	CSp1	Aerosol	**14.08**	**18.14**	**32.30**					
		CsI	14.45	18.80	32.34					
$MgAl_2O_4$	CSp2	Aerosol	**13.26**	**17.79**	**32.61**					
		CsI	14.07	17.91	32.31					

plied for the theoretical calculations. The spectrum calculated for the spherical particles exhibit a sharp-pointed peak with the narrowest bandwidth. As the particles become ellipsoidal shapes, the peak undergoes a red shift, and the bandwidth gradually broadens (CDE1 & CDE2). These calculations demonstrate the possible shape effect on the measured band profiles. The CR2 spectrum in Fig. 5 is between the spectra of the CDE1 and CDE2 in the 12-20 μm wavelength range. Fig. 4(c) images show that the CR2 particles have an irregular shape; however, the band profiles of the CR2 particles, especially at 23.5 and 28 μm are much closer to that calculated for near-spherical shapes. Conversely, although the CR4 particles are similarly of near-spherical shape (Fig. 4(e)), the CR4 measured band profile does not fit well with either the CDE1 or the CDE2 spectrum. A nearly trapezoidal profile is seen in the wavelengths between 13 and 19 μm. The short wavelength peak corresponds well to spherical particles. The long wavelength peak is not exactly reproduced by the CDE2. The same is true for the profile at longer wavelengths. As already mentioned, this behavior may be caused by the agglomerate effect because it is more difficult to separate particles as particles decrease in size. The effect of agglomeration is also clearly seen in the anatase spectra, specifically in the 12-25 μm band complex.

CA1 (Fig. 4(f)) and CA2 (Fig. 4(g)) have very similar particle conditions. They have a particle shape with rounded edges, forming an elongated and porous type of agglomerate, and micron size particles.

CA3 (Fig. 4(h)) particles which are nanometer-sized, on the other hand, form many close-packed agglomerates which produce a broadening effect on the band profile. Although the particle size of the CA3 and CA4 (Fig. 4(i)) samples are very much alike, the agglomerate state is different. Whereas CA3 particles form more close-packed agglomerates, CA4 is composed of not only close-packed agglomerates, but also a large amount of porous agglomerates. Consequently, the secondary band at 21 μm is much stronger for CA3.

The CAC1 aerosol spectrum, in contrast, has a peak at short wavelengths, indicating near spherical shape and a trapezoidal

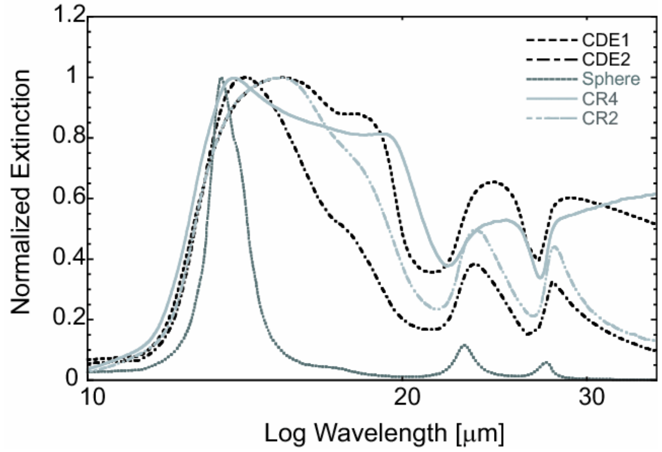

Fig. 5. Normalized extinction spectra of the two different rutile samples (CR2 & CR4) obtained by aerosol measurements are compared with three different calculated spectra (CDE & spheres) in air. (Note: CDE1 for equal weight of all ellipsoidal shapes & CDE2 for preferentially near-spherical particles)

profile because of stronger agglomeration.

Begemann et al. (1997) suggested that the 13 μm band profile of α-Al_2O_3 is susceptible to particle shape. The wavelength range between 13 and 20 μm of α-Al_2O_3 is sensitively affected by morphological effects as in the case of rutiles (Tamanai 2007). CAC1 (Fig. 4(n)) and CAC2 (Fig. 4(o)) samples differ in both the shapes and sizes of the particles. While the CAC1 particles have an irregular shape with rounded edges, CAC2 ones have an irregular shape with very sharp edges (like crushing a stone into small pieces by a hammer). As in the case of rutile (CR1 and CR2) samples, the sharp edged CAC2 particles give rise to a distinctive single peak at 14.9 μm in the aerosol measurements.

CSp1 (Fig. 4(r)) and CSp2 (Fig. 4(s)) particles form a large number of agglomerates with very similar agglomerate states. However, CSp2 is composed of near-spherical grains, whereas CSp1 contains large sharp-edged particles. It is plausible that the individual particle shape exerts a stronger influence on these spectra than the agglomerate state and particle sizes. In accordance with that expectation, the spherical shaped particles produce peaks at relatively shorter wavelengths and with narrower bandwidth compared to the sharp-edged ones (see also Fig. 5). The peak for CSp2 particles is located at 13.26 μm which is 0.82 μm red-shifted compared to the peak of CSp1.

In general, strong extinction peaks are known to originate in geometrical resonances of the particles. Strong bands rather than the weaker ones are tremendously influenced by morphological effects and these effects are seen also in this investigation. Unfortunately it is virtually impossible to quantify the relative importance of each morphological effect. A simulation study of shape effects will be published in a forthcoming paper (Mutschke et al. in prep.).

3.3. Quantitative measurements

We examine the extinction strengths caused by particle shapes and embedding media via CDE and Rayleigh calculations. The model spectra of forsterite, rutile, and spinel calculated in both vacuum and CsI media are shown in Fig. 6. All the quantitative spectra are affected by the CsI in the same way. The spectra in CsI medium exhibit a factor of approximately 1.5 higher extinction strengths than those in vacuum. The extinction strengths increase as the particle configuration becomes spherical (CDE1 → sphere). We checked by CDE calculations that apart from a roughly proportional change of the absolute magnitude, spectra of particles in vacuum have the same relative peak strength as in CsI.

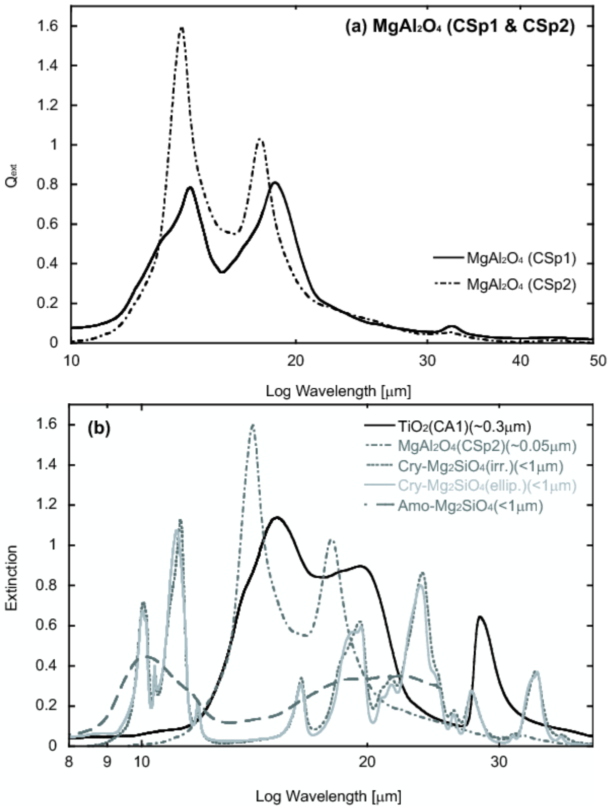

Fig. 7. (a) Extinction efficiency vs. wavelength of two $MgAl_2O_4$ spectra (CSp1 & CSp2) obtained by CsI pellet measurements. (b) Extinction vs. wavelength of five different spectra (CA1, CSp2, crystalline forsterites (irregular and ellipsoidal shaped particles), and amorphous Mg_2SiO_4) obtained by CsI pellet measurements.

A comparison between the two $MgAl_2O_4$ (CSp1 & CSp2) samples are shown in Fig. 7(a). Although identical amounts of samples are embedded in the CsI pellets, these spectra show an enormous difference of the peak strength in the spectrum. The extinction at 14 μm for CSp2 is almost twice as much as that of CSp1. It is probable that the difference in extinction between the CSp1 and CSp2 samples is chiefly caused by morphological effects, especially shape.

We compare the quantitative measured spectrum of amorphous and crystalline Mg_2SiO_4 (ellipsoidal and irregular shaped forsterites) with TiO_2 (CA1) and $MgAl_2O_4$ (CSp2) (Fig. 7(b)). In the legend of Fig. 7(b), the particle sizes are listed as well. These HTC spectra are of much stronger extinction strength than the amorphous Mg_2SiO_4 spectrum.

Note also that the extinction strengths of forsterite differ from the theoretical calculations for the CsI measured spectrum (Fig. 7(b)). As the forsterite particle shape becomes spherical, the strength of the 11 μm peak becomes stronger and more prominent than the others in the calculations, but the strength of spinel in the measured spectrum is in fact the strongest in this comparison. The peak position of measured ellipsoidal forsterite

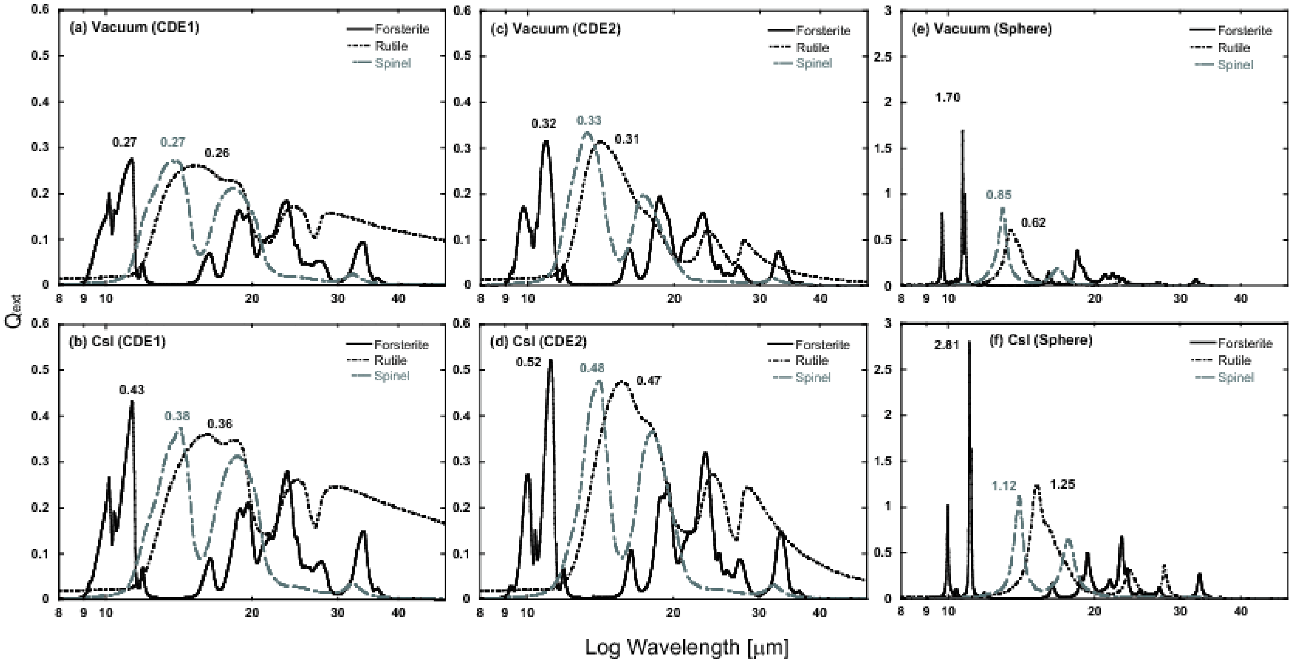

Fig. 6. Extinction efficiency vs. wavelength of forsterite, rutile, and spinel spectra in vacuum (upper plots) and CsI medium (bottom plots) obtained by CDE1 (a & b), CDE2 (c & d), and sphere (e & f) calculations (r=0.1 μm). Numerical extinction strengths at each peak are given in each plot.

takes place at 11.14 μm which is closer to the peak obtained by the calculation for spherical particles (11.06 μm) compared to that of irregular shaped forsterite (11.27 μm). The bandwidth of measured ellipsoidal forsterite is much broader than that of the calculated band profile, and the measured forsterite band profile does not contain any prominent peaks. On the other hand, the peak position of measured spinel is located at 14.07 μm whereas the calculated peak lies at 13.99 μm ($\Delta\lambda$=0.08 μm). The bandwidth of calculated spinel is slightly narrower than the measured one. However, the band profiles of the measured and calculated spinel spectra are comparable. This result directly affects the extinction strength. The ellipsoidal forsterite particles are not spherical enough to produce the stronger extinction strength compared to the spherical spinel. The greater extinction strength seen for forsterite is due to the shape effect of individual particles upon the extinction strength.

According to Millar (2004), amorphous silicates are conceivably the dominant species of grains, with a small amount of crystalline silicates in oxygen-rich AGB stars. As shown in Fig. 7(b), amorphous Mg_2SiO_4 produces an ineffective extinction feature. If the amount of crystalline Mg_2SiO_4 is much less than that of oxides, it may be possible to detect some pronounced features from oxide dust grains in mid-IR region even if amorphous Mg_2SiO_4 is abundant.

4. Astrophysical implication

We selected three AGB objects which exhibit strong 13, 19.5, and 28 μm features. ISO emission spectra of S Pav, Y UMa, and g Her are shown in Fig. 8 together with the spectra obtained by the aerosol measurements of anatase (CA1 & CA4), spinel (CSp2), tialite (Al_2TiO_5) and amorphous Mg_2SiO_4 (Tamanai et al. 2006b) in the wavelength range between 8 to 45 μm. Basic properties and detailed observed data analysis information of these AGB objects are given in Posch et al. (1999), Posch et al. (2002), and Fabian et al. (2001).

The emission spectra of S Pav and Y UMa (Fig. 8(a) & (b)) show a strong and broad 9-40 μm background. An 11 μm peak, which is clearly seen in both spectra, may originate from amorphous Al_2O_3 (Cami 2002). In contrast, the emission spectrum of g-Her (Fig. 8(c)) has a weaker background and a clear 10 μm amorphous silicate band (Millar 2004). The 10 μm band appears as a shoulder only in the spectra of S Pav and Y UMa. These spectra exhibit bands at 13, 16-22 (equally strong, with substructures), 28, and 32 μm (weak, especially in S Pav; apparently quite strong in g-Her). The relative strength of the bands may be a temperature effect.

A strong 13 μm feature appears in all three objects as well as 19.5 and 28 μm features. Anatase, spinel and tialite produce peaks around 13 μm, but the anatase (CA1) peak (13.1 μm) corresponds best with the 13 μm feature of the observed spectra. However, the 13 μm feature in the observed spectra is rather a prominent peak. It is possible that spinel (like CSp2) enhances the protuberance of the 13 μm peak.

As mentioned in Sec. 3.2, the wavelength range between 13 and 20 μm of the TiO_2 spectra is finely influenced by morphological effects. Fig. 8(d) and (e) show the two types of anatase spectra that exhibit different band profiles caused by morphological effects (Table 1). As the morphological state of the particles varies, the band profile is noticeably changed as well. Consequently, it may be that anatase particles with a different morphological state are able to enhance the 13 μm peak and/or to produce a clearer peak around 19 μm.

Additionally, we consider that tialite plays an important role in the observed spectra. When all these HTCs (Al_2O_3, TiO_2, $MgAl_2O_4$) are present in the same environment, tialite and more complex titanate dust grain formation is expected (see sec. A.6.). According to Buscaglia et al. (1996), $MgAl_2O_4$ and TiO_2 react into $Mg_{0.5}AlTi_{1.5}O_5$ particles which are formed at a temperature above $\approx$1423 K. These behave like nuclei for further titanate (e.g. $AlTiO_3$, $MgTiO_3$, $MgTi_2O_5$, Al_2TiO_5) formation and growth. Consequently, $MgAl_2O_4$ produces an effect on the mechanism of Al_2TiO_5 formation. If spinel dust grains exist in an environment, Mg containing titanate may form (see also Posch et al. 2003). This is also an interesting point to associate with a subsequent condensation process in the outflow of AGB stars. From the spectroscopic point of view, although the 13 μm peak of tialite is not as prominent of the peak in CSp2, this peak is expected to enhance the strength of the emission in the observed spectra.

As to the peak at 19.5 μm, none of the measured spectra produced a peak adequate to explain the observed spectra. However, the observed peak at 19.5 μm might be contributed by anatase dust grains because the three observed spectra in Fig. 8 have a common feature, namely that the emission strength of the 13 μm feature correlates with that of the 19.5 μm peak. g-Her (Fig. 8(c)) shows the narrowest and sharpest 13 and 19 μm peaks among the observed spectra while S Pav exhibits a broader peak at 13 μm, and then the 19.5 μm peak becomes more like a small shoulder. Sloan et al. (2003) discussed about the correlated dust features at 13, 20 and 28 μm and concluded that the 20 and 28 μm features originated in silicates. Posch et al. (2002) proposed that the 19.5 μm feature carrier would be $Mg_{0.1}Fe_{0.9}O$ in relation to the band profiles (the band width, shape and position), but the formation of $Mg_{0.1}Fe_{0.9}O$ in the circumstellar environment is not yet well understood. We expect that all three peaks (13, 19.5 and 28 μm) come from a single source. The observed spectra undergo a slight change in the band profiles (e.g. peak shift, band broadening, and the strength of extinction feature) by other relatively less influential sources. In order to clarify the source of the 19.5 μm feature, it is necessary to take morphological effects into account and to carry out further investigation.

Another point to be investigated is the band feature beyond 19.5 μm. The observed spectra exhibit a gradual fall beyond 19.5 μm, and excessive extinction features cannot be seen in this wavelength region. In fact, rutile is the most stable material out of the three crystalline phases of TiO_2 (see sec. A.2.). However, the anatase spectra fit better with these observed spectra since they do not show any peaks around 25 μm, unlike the rutile spectra (Fig. 4(b)-(e)). The minor peaks circled ($\approx$ 28 μm) in Fig. 8(a-c) fit well with the anatase features (CA1 & CA2) as well as with tialite.

Furthermore, as mentioned above, the 10 μm feature originates from amorphous silicate (Millar 2004). In this investigation, the amorphous Mg_2SiO_4 spectrum obtained by aerosol measurement compares well with the 10 μm feature, especially for the spectrum of g-Her.

5. Summary and discussions

Spectroscopic extinction measurements of HTCs are performed in the wavelength range between 10 and 50 μm by making use of the aerosol technique in order to obtain the band profiles without any medium effect. We focus particularly on morphological effects on the measured spectra to obtain a new perspective on the 13, 19.5, and 28 μm carriers in the spectra of AGB stars. We summarize the main results of this paper as follows:

- There is a tendency for peaks to appear at longer wavelengths due to the influence of the medium on the surface modes. The effect is expected (Bohren & Huffman 1983), but is very strong for many HTCs. The maximum peak position difference between the aerosol and CsI pellet measurement is 3.20 μm in wavelength in the case of the TiO_2 anatase (CA4) sample.
- Particles which have spherical or roundish shapes produce larger differences between the spectra measured by the aerosol and the CsI pellet techniques as compared to the irregular shaped particles.
- Roundish grains tend to produce double peaked (rectangular) profiles in comparison with irregular shaped grains.
- The agglomerate state may strongly influence the strength of the strong bands. The extinction band profile between 13 and 19.5 μm undergoes a substantial change for different agglomerate states (rutile & anatase).
- Although band profiles are influenced by the morphological effects, it is practically unfeasible to quantify the relative importance of each morphological effect.
- In comparison to TiO_2, Al_2O_3 creates a larger disparity in the band profiles. In particular, three different crystal structures have been detected by a X-ray diffraction analysis in χ-δ-κ-Al_2O_3 that produce 25 discernible peaks up to 45 μm.
- The absolute strength of extinction strongly depends on chemical composition and particle morphology. Spherical shaped nano-sized spinel shows the most effective extinction in all samples investigated here.
- Through the comparison of the observed emission in AGB spectra and the aerosol spectra, we find that primarily the roundish edged anatase (CA1) is anticipated to contribute to the 13 and 28 μm peaks. Spherical shaped nano-sized spinel (CSp2) plays a role in intensifying the 13 μm peak as well as tialite (Al_2TiO_5). The carrier for the peak at 19.5 μm could not be identified well in this investigation. However, as a possibility, the 19.5 μm peak might be produced by the same source (anatase) when the particle morphology and temperature are taken into account.

In fact, titanium is a significantly less abundant metal by a factor of 400, compared to Si (Cameron 1973). Posch et al. (2003) noted that rutile and anatase in the 13 μm region are about 40 times more effective absorbers than amorphous silicate, and they predicted that the most prominent TiO_2 emission will be about 1/10th as strong as the silicate dust emission. Likewise, our CsI pellet measurements exhibit very similar results, and show that anatase radiates approximately 8.5 times more efficiently than amorphous Mg_2SiO_4. However, there still a huge difference between the abundance proportions of Ti and Si. If the solar abundance can be applied in the AGB star environments, the Ti abundance remains unclear.

The abundance of possible condensates has been calculated under the assumption of chemical equilibrium. Chemical equilibrium cannot apply to the dust condensation process in circumstellar dust shells since grain formation takes place in a non-equilibrium kinetic process. The non-equilibrium calculations of Ferrarotti & Gail (2001) showed that a different mixture of minerals form compared to an equilibrium calculation. Although the equilibrium assumption may be very convenient as an approximation to understand possible condensates present in certain conditions, the detailed condensation process can only be explored with non-equilibrium calculations. More dependable non-equilibrium condensation process results are required to study further dust grain formation in the circumstellar outflow of AGB stars.

While having a precise knowledge of the absolute strength of extinction for each substance is essential to identify the dust grains present in dust shells, it is also very important to understand heterogeneous dust grain properties. We have concentrated only on homogeneous dust grain investigations here. Each sample has unique properties which determine the agglomerate state. The agglomeration of non-spherical particles increases in comparison to spherical particles with the same volume because the non-spherical particles have a larger surface area which leads to more collisions by Brownian motion (e.g. Hinds 1999; Blum et al. 2000; Krause & Blum 2004; Paszun & Dominik 2006). As the particle shape irregularity becomes much more complicated, the agglomeration effect will be more significant. According to a theoretical calculation by Zebel (1966), ellipsoidal particles have a 35 % higher agglomeration coefficient than spherical ones with the same volume. Hence, heterogeneous grains make both the thermal and kinematic agglomeration processes more complicated. An experimental heterogeneous dust grain investigation is indispensable to address this problem.

By way of another approach, we will attempt to mix crystalline and amorphous samples together so as to observe how these mixed particles interact with each other and produce an effect on the band profiles. We focused only on crystalline dust particles in this investigation, since we presume that the 13 μm peak mainly originates from a crystalline species. Unlike crystalline materials, amorphous particles tend to produce broader bands due to the range of bond lengths and angles of atoms in the amorphous structure (Jäger et al. 2003). However, as the three observed AGB spectra (Fig. 8) show broad peaks between 10 and 13 μm, it is recognizable that amorphous materials (e.g. silicates) take part in the spectra. Posch et al. (2002) proposed that amorphous Al_2O_3 contributes a broad "continuum emission" (g Her, Y UMa, V1943 Sgr) in the wavelength range between 11 and 15 μm. Thus, it is interesting to examine how the strong crystalline features are weakened by amorphous materials by changing the quantity of each material.

During aerosol measurements, the large and compact agglomerates start to be deposited in the cell; therefore, only the remaining small and fluffy agglomerates can keep flying in the cell for a long time. These aerosol spectra reflect the difference in bandwidth. A spectrum from a sample which contains more large agglomerates shows broader bands. However, the variation of these spectra is not very strong. Since the particle densities are too low (10^6 particles/cm^3) and the gas pressure is too high, these experiments are not a suitable environment to observe the growth of particles by agglomeration.

Concerning the quantitative aspects of the aerosol measurements, it is extremely difficult to obtain the exact mass concentration in the cell during the measurements. One of the possible ways to solve this problem is to derive the mass through a theoretical analysis. The extinction efficiency of small-sized particles can be calculated by means of the form-factor distribution (Min et al. 2006) which can then be fitted to the measured spectrum. A forthcoming paper will include more discussion of these concepts (Mutschke et al. in prep.).

Identification of dust grains in astrophysical environments is not straightforward. The band profiles are strongly influenced by physical and chemical factors of the dust grains which interact with each other and make the identification all the more complicated. It is essential to carry out condensation experiments and more detailed non-equilibrium condensation theoretical approaches for the circumstellar dust shells around AGB stars.

The infrared extinction spectra database can be found at *http://elbe.astro.uni-jean.de*. The database includes the numerical extinction efficiency data obtained by both the aerosol and CsI pellet measurements, SEM and TEM images, basic properties, plots, and peak positions of each sample.

Acknowledgements. We express to the members of the pathology department at FSU Jena, Dr. S. Nietzsche, F. Steiniger, and C. Kamnitz our gratitude for the technical support of the TEM and SEM. We are thankful to Dr. D.R. Alexander at ISU and Dr. D. Hilditch at FSU Jena (TPI) for proofreading and insightful opinions and comments. We are grateful to G. Born for her assistance with sample preparation and W. Teuschel for his technical support of our experimental devices. Our project has been supported by Deutsche Forschungsgemeinschaft (DFG) under the grant MU 1164/6.

References

Allard, F., Hauschildt, P.H., Alexander, D.R., Tamanai, A., & Schweitzer A. 2001, ApJ, 556, 357
Åsbrink, S., & Magnéli, A. 1959, Acta Cryst., 12, 575
Barker, A.S.Jr. 1963, Phys.Rev., 132, 1474
Begemann, B., Dorschner, J., Henning, Th., & Mutschke, H. 1997, ApJ, 476, 199
Bhattacharya, I.N., Das, S.C., Mukherjee, P.S., Paul, S., & Mitra, P.K. 2004, Scand.J.Metall., 33, 211
Blum, J., Wurm, G., Poppe, T., et al. 2000, Phys.Rev.Lett., 85, 2426
Brandes, E.A., & Brook, G.B. 1992, Smithells Metal Reference Book (Butterworth-Heinemann Ltd., Oxford)
Bohren, C.F., & Huffman, D.R. 1983, Absorption and Scattering of Light by Small Particles (John Wiley & Sons Inc., N.Y.)
Buscaglia, V., Delfrate, M.A., Leoni, M., & Bottino, C. 1996, J.Mater.Sci, 31, 1715
Cameron, A.G.W. 1973, Space Sci. Rev., 15, 121
Cami, J. 2002, Ph.D. thesis, University of Amsterdam, The Netherlands
Chihara, H., Tsuchiyama, A., Koike, C., & Sogawa, H. 2000, in ASP Conference Series Disks, Planetesimals and Planets, eds. F. Garzon, C. Eiroa, D. de Winter, & T.J. Mahoney, Vol.219, 150
Chihara, H., Koike, C., Tsuchiyama, A., Tachibana, S., & Sakamoto, D 2002, A&A, 391,267
Chu, Y.T., Bates, J.B., White, C.W., & Farlow, G.C. 1988, J.Appl.Phys., 64, 3727
Clément, D., Mutschke, H., Klein, R., & Henning, Th. 2003, ApJ, 594, 642
Coelho, A.C.V., Santos, H.de S., Kiyohara, P.K., Marcos, K.N.P., & Santos, P.de S. 2007, Matar.Res., 10, 183
DePew, K., Speck, A., & Dijkstra, C. 2006, ApJ, 640, 971
Draine, B.T. 1988, ApJ, 333, 848
Dorschner, J., Friedemann, C., & Gürtler, J. 1978, Astron.Nachr., 299, 6
Douglas, B.E., & Ho, S.M. 2006, Structure and Chemistry of Crystalline Solids (Springer, N.Y.)
Fabian, D., Posch, Th., Mutschke, H., Kerschbaum, F., & Dorschner 2001, A&A, 373, 1125
Ferguson, J.W. et al. 2005, ApJ, 623, 585
Ferrarotti, A.S., & Gail, H.-P. 2001, A&A, 371, 133
Freundenberg, B., & Mocellin, A. 1987, J.Am.Ceram.Soc., 70, 33
Freundenberg, B., & Mocellin, A. 1988, J.Am.Ceram.Soc., 71, 22
Fujimura, T. et al. 1989, High Pressure Research, 1, 213
Gail, H.P., & Sedlmayr, E. 1998, Faraday Discuss., 109, 303
Gail, H.P., & Sedlmayr, E. 1999, A&A, 347, 594
Gervais, F. 1991, Handbook of Optical Constants of Solids II, ed. Palik, E.D. (Academic Press Inc., Orland) 1035
Gillet, P., Guyot, F., Price, G.D., Tournerie, B., & Le Cleach, A. 1993, Phys. Chem. Minerals, 20, 1993
Gusev, A.I. 1991, phys.stat.sol (b), 163, 17
Glaccum, W 1995, in ASP Conf. Proc. 73, Proc. Airborne Astronomy Haas, ed. J.A. Davidson, & E.F.Erickson (ASP, San Francisco), 395
Greshake, A., Bischoff, A., & Putnis, A. 1996, Lunar & Planetary Science, 27, 463
Greshake, A., Bischoff, A., & Putnis, A. 1998, Meteoritics & Planetary Science, 33, 75
Grossman, L., & Larimer, J.W., 1974, Rev. of Geophys.& Space Phys., 12, 71
Habing, H.J., & Olofsson, H. 2004, Asymptotic Giant Branch Stars, ed. H.J. Habing, & H. Olofsson (Springer-Verlag, N.Y.), 1
Henning, Th., & Mutschke, H. 2000, in Thermal Emission Spectroscopy and Analysis of Dust, Disks, and Regoliths, eds. M.L. Sitko, A.L. Sprague, and D.K. Lynch, 196, 253
Hinds, W.C. 1999, Aerosol Technology: Properties, Behavior, and Measurement of Airborne Particles, (John Wiley & Sons Inc., N.Y.)
International Advanced Materials 1999, http://www.iamaterials.com/compounds /titaniumoxide4.htm
Jäger, C., Mutschke, H., Begemann, B., Dorschner, J., & Henning, Th. 1994, A&A, 292, 641
Jäger, C., Dorschner, J., Mutschke, H., Posch, Th., & Henning, Th. 2003, A&A, 408, 193

Jeong, K.S., Winters, J.M., & Sedlmayr, E. 1999, in IAU symposium Asymptotic Giant Branch Stars, eds. T. LeBerte, A. Lebre, & C. Waelkens, Nr.191, 233

Jianu, A., Stanciu, L., Groza, J.R., Lathe, Ch., & Burkel, E., 2003, Nucl.Instrum.Methods B, 199, 44

Jun, S.G., Bursill, L.A., Yoshida, K., Yamada, Y., & Ota, H. 1984, Acta Cryst., B40, 549

Klein, C., & Hurlbut, C.S.Jr. 1993, Manual of Mineralogy, (John Wiley & Sons, Inc., N.Y.)

Koike, C., Hasegawa, H., Asada, N., & Hattori, T. 1981, Ap&SS, 79, 77

Koike, C., & Hasegawa, H. 1987, Ap&SS, 134, 361

Koike, C. et al. 1995, Icarus, 114, 203

Kozasa, T., & Sogawa, H. 1997, Ap&SS, 255, 437

Krause, M., & Blum, J. 2004, Phys.Rev.Lett., 93, 021103

Kurumada, M., Koike, C., & Kaito, C. 2005, MNRAS, 359, 643

Lide, D.R. 1990, CRC Handbook of Chemistry and Physics (CRC Press Inc., Boston)

Linsebigler, A.L., Lu, G., & Yated, J.T.Jr. 1995, Chem. Rev., 95, 735

Loewenstein, E.V., Smith, D.R., & Morgan, R.L. 1973, Applied Optics, 12, 398

Lucovsky, G., Sladek, R.J., & Allen, J.W. 1977, Phys. Rev. B, 16, 5452

Mackowski, D.W., & Mishchenko, M.I. 1996, J.Opt.Soc.Am.A, 13, 2266

Mie, G. 1908, Ann.Phys., 25, 377

Millar, T.J. 2004, Asymptotic Giant Branch Stars, ed. H.J. Habing, & H. Olofsson (Springer-Verlag, N.Y.), 247

Min, M., Hovenier, J.W., de Koter, A., Waters, L.B.F.M., & Dominik, C. 2005, Icarus, 179, 158

Min, M., Hovenier, J.W., Dominik, C., de Koter, A., & Yurkin, M.A. 2006, J. Quant. Spec. Radiat. Transf., 97, 161

Mishchenko, M.I. 1990, Ap&SS, 164, 1

Mo, S.-D, & Ching, W.Y. 1995, Phy.Rev.B, 51, 13023

Muraishi, H. 2004, Basic Solid State Chemistry for Inorganic Materials (Sankyo Shuppan Inc., Tokyo)

Nittler, L.R., Alexander, C.M.O'D., Stadermann, F.J., & Zinner, E.K. 2005, in 36^{th} Annual Lunar and Planetary Science Conference, Abst. No.2200

Nittler, L.R., et al. 2008, ApJ, 686, 1524

Onaka, T., de Jong, T., & Willems, F.J. 1989, A&A, 218, 169

Onoda, M. 1998, J. Solid State Chem., 136, 67

Orofino, V., et al. 1991, A&A, 252, 315

Ossenkopf, V., Henning, Th., & Mathis, J.S. 1992, A&A, 261, 567

Papoular, R., Cauchetier, M., Begin, S., & LeCaer, G. 1998, A&A, 329, 1035

Paszun, D., & Dominik, C. 2006, Icarus, 182, 274

Perry, C.H., & Khanna, B.N. 1964, Phys.Rev.A, 135, 408

Posch, Th., et al. 1999, A&A, 352, 609

Posch, Th., Kerschbaum, F., Mutschke, H., Dorschner, J., & Jäger, C. 2002, A&A, 393, L7

Posch, Th. et al. 2003, ApJS, 149, 437

Potter, D.K., & Ahrens, T.J. 1994, Geophys.Res.Lett., 21, 721

Preudhomme, J., & Tarte, P. 1971, Spectrochimica Acta, 27A, 961

Purcell, E.M., & Pennypacker, C.R. 1973, ApJ, 186, 705

Querry, M.R. 1985, Optical Constants (Chemical Research and Development Center, Maryland)

Reade Advanced Materials 1997, http://www.reade.com/Products/Minerals_and_Ores/anatase.html

Redfern, S.A.T., & Carpenter, M.A. 2000, Transformation Processes in Minerals (Mineralogical Society of America, Washington DC)

Ribarsky, M.W. 1985, Handbook of Optical Constants of Solids, ed. Palik, E.D. (Academic Press Inc., Orland), 795

Rohrer, G.S. 2001, Structure and bonding in crystalline materials (Cambridge Univ. Press, Cambridge)

Saalfeld, H. 1958, Clay Min.Bull., 3, 249

Saniger, J.M. 1995, Materials Letters, 22, 109

Santos, P.S., Santos, H.S., & Toledo, S.P. 2000, Mater.Res., 3, 104

Schmocker, U., Boesch, H.R., & Waldner, F. 1972, Phys. Lett., 40A, 237

Sedlmayr, E. 1994, in Molecules in the Stellar Environment, ed. U.G. Jorgensen, 428, 163 (Springer-Verlag, Berlin)

Sharp, C.M., & Huebner, W.F. 1990, ApJS, 72, 417

Sloan, G.C., Kraemer, K.E., Goebel, J.H., & Price, S.D. 2003, ApJ, 594, 483

Speck, A.K., Barlow, M.J., Sylvester, R.J., & Hofmeister, A.M. 2000, A&AS, 146, 437

Stanciu, L.A., Groza, J.R., Jitianu, A., & Zaharescu, M. 2004, Mater.Manuf.Process, 19, 641

Straumanis, M.E., & Ejima, T. 1962, Acta Cryst., 15, 404

Streitz, F.H, & Mintmire, J.W. 1999, Phys.Rev.B, 60, 773

Stroud, R.M, Nittler, L.R., & Alexander, C.M.O'D. 2004, Sci, 305, 1455

Tamanai, A., Mutschke, H., Blum, J., Neuhäuser, R. 2006a, J. Quant. Spec. Radiat. Transf., 100, 373

Tamanai, A., Mutschke, H., Blum, J., & Meeus, G. 2006b, ApJ, 648, L147

Tamanai, A. 2007, Ph.D. thesis, FSU Jena, Germany

Tropf, W.J., & Thomas, M.E. 1991, Handbook of Optical Constants of Solids II, ed. Palik, E.D. (Academic Press Inc., Orland), 883

Wefers, K., & Misra, C. 1987, Oxides and Hydroxides of Aluminum (Alcoa Research Laboratories, USA)

Wells, A.F. 1991, Structural Inorganic Chemistry (Clarendon Press, Oxford)

Woignier, T., Lespade, P., Phalippou, J., & Rogier R. 1988, J.Non-Cyst.Solids, 100, 325

Zebel, G. 1966, Coagulation of Aerosols, in Aerosol Science, ed. C.N. Davis, (Academic Press, N.Y.), 31

Zribi, M., Kanzari, M., & Rezig, B. 2008, Thin Solid Films, 516, 1476

Appendix A: Physical properties of oxides

A.1. TiO

Titanium oxide, TiO_x ($0.7 \le x \le 1.25$), forms in a cubic crystal structure (Jun et al. 1984). TiO is the one-to-one composition of the TiO_x series and has a defective NaCl crystal structure which is composed of identical numbers of random vacancies in the cation and anion sites in cubic symmetry at temperatures higher than 1273 K (Fujimura et al. 1989; Wells 1991). However, the cubic crystal structure of TiO_x can be transformed into various ordered structures such as cubic, tetragonal, orthorhombic, and monoclinic lattices. The transformation depends strongly on oxygen content and temperature conditions (Jun et al. 1984; Gusev 1991). The melting point of TiO is 2023 K (Lide 1990) which is the lowest temperature among the Ti-compounds investigated here.

Solid TiO forms from TiO_2 and H_2 gases through the chemical reaction in the circumstellar outflow of M stars

$$TiO_2(\text{gas}) + H_2 \longrightarrow TiO(\text{solid}) + H_2O$$

(Gail & Sedlmayr 1998).

A.2. TiO_2

Titanium dioxide (titanium(IV) oxide or titania) (TiO_2) occurs in three different crystal structures, which are stable at atmospheric pressure. They are rutile, anatase, and brookite. Although the anatase and brookite phases are stable at lower temperature than rutile, both transform to rutile at approximately 1188 K (anatase) and 1023 K (brookite) (Brandes & Brook 1992). Rutile is the most stable form of the three phases. It belongs to the tetragonal crystal system and has a melting point at 2123 K (Lide 1990). Anatase is a member of the tetragonal crystal system as well. The density of anatase is approximately 10 % less than that of rutile (Linsebigler et al. 1995). The melting point of anatase, which is about 2108 K (Reade Advanced Materials 1997), is slightly lower than that of rutile.

In the crystal structure system, rutile and anatase consist of the basic structural unit of the TiO_6 octahedron. Each Ti^{+4} ion occupies the center of the oxygen octahedra, so that it is surrounded by 6 O^{2-} ions. Conversely, since each O^{2-} ion is enclosed by 3 Ti^{4+} ions, the Ti:O ratio will be 3:6. In both cases, TiO_2 octahedra are distorted, and anatase has more distortions than rutile (see details in e.g. Mo et al. 1995; Klein & Hurlbut 1993; Muraishi 2004).

TiO_2 solid would form from the gas phase via

$$TiO_2(\text{gas}) \longrightarrow TiO_2(\text{solid})$$

(Gail & Sedlmayr 1998). Solid TiO_2 (rutile) contributes to Al_2TiO_5 formation (see 2.2.6).

In addition, when a deposited TiO thin film underwent annealing in air, anatase and rutile structures have been shown at a temperature of 793 K (Zribi et al. 2008), which indicates possible TiO_2 formation from TiO via an annealing process.

The optical properties of TiO_2 (rutile, brookite, anatase) are found in Posch et al. (2003).

A.3. Ti_2O_3

Dititanium trioxide (Ti_2O_3) has a trigonal crystal structure. O^{2-} ions are positioned in a hexagonal close-packed structure and Ti^{3+} ions occupy 2/3 of the octahedral interstices (Wells 1991). Ti_2O_3 has a corundum-type structure (see sec. A.7.) at all temperatures (Straumanis & Ejima 1962). The melting point is 2503 K, which is much higher than that of TiO_2.

A possible solid Ti_2O_3 formation pathway from the gas phase is

$$2TiO_2(gas) + H_2 \longrightarrow Ti_2O_3(solid) + H_2O$$

(Gail & Sedlmayr 1998). Reflectance measurements of a single Ti_2O_3 crystal sample at room-temperature have been performed by Lucovsky et al. (1977). The measurements were made for the two primary polarizations, namely with the crystalline c-axis perpendicular and parallel to the plane of incidence. The TO-phonon frequencies obtained with the perpendicular measurements were 19.6, 22.2, 26.6, and 35.7 μm and 18.6, 19.9, 25.6, and 35.6 μm for the LO modes. Likewise, the parallel measurements of the TO-phonon frequencies were shown at 22.3 and 29.2 μm, and 18.1 and 28.5 μm for the LO modes (see also Posch et al. 2003).

A.4. Ti_3O_5

Trititanium pentoxide is one of the Ti_nO_{2n-1} (n≥4) series. Åsbrink & Magnéli (1959) ascertained the Ti_3O_5 crystal structure at room temperature to be monoclinic. The crystal structure of Ti_3O_5 is composed of a three dimensional array of TiO_6 octahedra sharing edges and vertices (Wells 1991). However, Ti_3O_5 is also a substance which undergoes phase transitions of crystal structures during heating. A transition from monoclinic to orthorhombic phases has been seen at a temperature of 514 K (Onoda 1998).

Ti_3O_5 may form via the chemical reaction

$$3TiO_2(gas) + H_2 \longrightarrow Ti_3O_5(solid) + H_2O$$

(Gail & Sedlmayr 1998). The melting point of Ti_3O_5 is 2033 K (International Advanced Materials 1999) which is slightly lower than anatase and rutile. The stretching vibration of TiO_6 octahedra takes place in the wavelength range between 4.3 and 16.7 μm (600-700 cm^{-1}) (Gillet 1993) similarly to other Ti-compounds.

A.5. $CaTiO_3$

According to the relative abundances of dust grain calculations (sec. 2.3) (Fig. 2), $CaTiO_3$ (perovskite) appears at approximately 1700 K in chemical equilibrium before a large quantity of silicates starts to condense out of the gas. Solid perovskite may form via the chemical reaction

$$TiO_2(gas) + Ca + H_2O \longrightarrow CaTiO_3(solid) + H_2.$$

Ca exists as a free atom in the gas phase because Ca atoms are not able to form high bond energy molecules (Gail & Sedlmayr 1998). The melting point of perovskite is approximately 2248 K (Alfa Aesar Catalog) which is the second highest value among Ti-compounds.

Perovskite has an orthorhombic crystal system and a face centered cubic lattice (fcc) (e.g. Redfern & Carpenter 2000). Eight smaller Ti^{+4} cations are located at each corner of the cubic structure, and the large Ca^{+2} cation occupies the center. Twelve O^{2-} anions are positioned between each Ti^{4+} cation. Thus, the Ca^{2+} cation is surrounded by the 12 O^{2-} and 8 Ti^{4-} cations with a coordinate distance to form the cubic close-packed structure which is sustained only if the 12-fold coordinated Ca^{2+} cation is larger than oxygen. Otherwise, the cubic crystal structure undergoes a distortion to transform into other crystal forms such as octahedra, tetragonal, orthorhombic, and monoclinic forms depending on the temperature. Once the face-centered cubic lattice loses its shape due to a change in temperature down to the Curie point, perovskite becomes a ferroelectric material that has a very high dielectric constant (e.g. Douglas & Ho 2006). The origin of $CaTiO_3$ IR absorption mainly arises from Ti-O stretching modes around 18.2 μm (550 cm^{-1}) and 22.5 μm (445 cm^{-1}), Ti-O-Ti bending mode at 55.6 μm (180 cm^{-1}), and the cation-TiO_3 lattice mode at 66.7 μm (150 cm^{-1}) (Perry & Khanna 1964).

Posch et al. (2003) derived optical constants of a natural $CaTiO_3$ crystal from reflectance measurements.

A.6. Al_2TiO_5

We considered that aluminum titanate (tialite or Al_2TiO_5) is a very interesting species to investigate, though it has not been discovered yet in any astronomical objects. Al_2TiO_5 can be formed above its equilibrium formation temperature, 1553 K (Freundenberg & Mocellin 1987, 1988). The formation of Al_2TiO_5 via the endothermic reaction would be

$$\alpha\text{-}Al_2O_3(corundum) + TiO_2(rutile) \longrightarrow \beta\text{-}Al_2TiO_5$$

(e.g. Woignier et al. 1988; Jianu et al. 2003). The melting point of Al_2TiO_5 is rather high (2133 K), as for Al_2O_3 and TiO_2 (Jianu et al. 2003). Although it is possible to maintain Al_2TiO_5 under metastable conditions at room temperature, the decomposition takes place at a temperature above 1123 K (Woignier et al. 1988). The reaction between corundum and rutile into Al_2TiO_5 begins at 1473 K. As the temperature increases to 1523 K, Al_2TiO_5 dominates in quantity (Jianu et al. 2003). Al_2TiO_5 belongs to the orthorhombic pseudobrookite-type crystal structure, which is composed of MO_6 octahedra sharing edges and vertices (M denotes metal) (Wells 1991). Ti-O and Al-O vibrations induce absorption at wavelengths between 13.3 and 25 μm (750-400 cm^{-1}). In detail, the stretching modes from octahedral AlO_6 appear between 13.3 and 16.7 μm (750-600 cm^{-1}), and the bending mode occurs approximately at 22.2 μm (450 cm^{-1}). By the same token, TiO stretching vibration modes are induced below 13.7 μm (730 cm^{-1}) in wavelength and tetrahedral coordinated Al-O produces peaks around 11.8 to 13.3 μm (850-750 cm^{-1}) (e.g. Preudhomme & Tarte 1971; Stanciu et al. 2004).

While Al_2TiO_5 may be sufficiently less abundant to not be visible in observed spectra, the formation of Al_2TiO_5 is possible via the chemical reaction of corundum and rutile.

A.7. Al_2O_3

Aluminum oxides crystallize into the form of corundum (α-Al_2O_3), which is the second hardest natural mineral. This hardness might be caused by the strong and short O-Al ionic bonds which attract O^{2-} ions and Al^{3+} ions close together in order to form a tremendously hard and dense close-packed crystal structure. α-Al_2O_3 is formed from aluminum hydroxides via many phase transitions by increasing calcination temperature. Take boehmite (AlO(OH)), for instance. The dehydration reaction pathway of boehmite is that it is first transformed into γ-Al_2O_3 (750 K) → δ-Al_2O_3 (1050 K) → θ-Al_2O_3 (≈ 1200 K) → α-Al_2O_3 (≈ 1300 K) (Wefers & Misra 1987). δ-Al_2O_3 has a tetragonal crystal structure like γ-Al_2O_3. On the one hand, in the dehydration reaction pathway of gibbsite ($Al(OH)_3$) is first changed to χ-Al_2O_3 (473-1173 K) → κ-Al_2O_3 (1173-1273 K) → α-Al_2O_3 (> 1273 K) (Coelho et al. 2007). κ-Al_2O_3 has hexagonal and orthorhombic crystal structures whereas the crystal systems of χ-Al_2O_3 are hexagonal and cubic (Bhattacharya et al. 2004). All the phases are metastable polymorphs of transition Al_2O_3 except α-Al_2O_3 which is always the end product. A reverse transition is also able to produce one or more metastable or transition Al_2O_3 molecules. γ-Al_2O_3 is the most common resultant from α-Al_2O_3 by cooling (Santos et al. 2000).

α-Al_2O_3 has a rhombohedral (or trigonal) crystal structure and is considered to be one of the early condensation species in a cooling gas environment of solar composition (Begemann et al. 1997). The melting point is in the range between 2273 and 2303 K (Lide 1990). In the crystal structure of α-Al_2O_3, the O^{2-} ions are arranged in a hexagonal close-packing structure, and the Al^{3+} ions occupy 2/3 of the octahedral interstices. One Al^{3+} ion is surrounded by 6 O^{2-} ions whereas one O^{2-} ion is enclosed within 4 Al^{3+} ions. Thus, the Al:O ratio will be 4:6 (e.g. Muraishi 2004).

γ-Al_2O_3 has a tetragonal crystal structure (Saalfeld 1958). γ-Al_2O_3 is a so-called "defect-spinel" because it has basically the same structure as spinel (e.g. Streitz & Mintmire 1999). Since γ-Al_2O_3 does not have Mg cations, Al cations occupy the Mg sites. As a result, the stoichiometry becomes Al_3O_4. It is necessary to remove 8/3 Al^{3+} ions from the 24 ions available in the spinel unit cell in order to correct the stoichiometry. Then, the unit cell contains 96 O^{2-} ions, 64 Al^{3+} ions, and 8 spinel cation vacancies. These vacancies are randomly distributed; exact locations have not been verified (e.g. Streitz & Mintmire 1999).

The equilibrium between a condensed phase and vapor phase can be represented in the case of α-Al_2O_3 as

$$2\mathrm{Al(gas)} + 3\mathrm{O(gas)} \longrightarrow \alpha\text{-}\mathrm{Al_2O_3(solid)}$$

(Grossman & Larimer 1974).

Al-O vibrations are induced in the mid-IR region (Begemann et al. 1997). LO modes were confirmed around 15.74, 17.57, 22.62, and 25.97 μm (635, 569, 442, and 385 cm^{-1}) with the electric field polarized perpendicular to the c-axis (ordinary ray) whereas LO modes around 11.11, 16.0, 20.83, and 25.77 μm (900, 625, 480, and 388 cm^{-1}) were observed with the ordinary ray. Likewise, the TO mode peaks at approximately 15.29, 17.15, and 25.00 μm (654, 583, and 400 cm^{-1}) appeared with the electric field polarized parallel to the c-axis (extraordinary ray). The LO modes of the extraordinary ray could be detected at about 11.48 and 19.53 μm (871 and 512 cm^{-1}) (see details in Barker 1963). Especially for γ-Al_2O_3, there exist vibrational frequencies in the range from 12.5 to 14.29 μm (680-500 cm^{-1}) and from 14.71 to 20 μm (800-700 cm^{-1}) (Saniger 1995).

Optical properties of various α-Al_2O_3 samples have been analyzed by many groups (e.g. Barker 1963; Loewenstein et al. 1973; Querry 1985; Gervais 1991) as well as γ-Al_2O_3 (e.g. Chu et al. 1988; Koike et al. 1995), δ- and θ-Al_2O_3 (Kurumada et al. 2005), and amorphous Al_2O_3 (e.g. Chu et al. 1988; Begemann et al. 1997).

A.8. $MgAl_2O_4$

$MgAl_2O_4$ (spinel) is known to be an important ferromagnetic material, which has very high permeability (e.g. Douglas & Ho 2006) and a cubic close-packed anion arrangement (e.g. Rohrer 2001) like most metallic crystals. The general formula of the spinel group can be described as XY_2O_4. X would be replaced with Mg^{2+}, Fe^{2+}, Ti^{4+}, Zn^{2+}, or Mn^{2+}. Y may be occupied by Al^{3+}, Fe^{3+}, Fe^{2+}, or Cr^{3+}.

In the case of magnesium aluminum spinel ($MgAl_2O_4$), the oxygens form a face-centered cubic closed-packed array along planes in the structure. Then, Mg^{2+} ions are placed in tetrahedral interstices (1/8 occupied) whereas Al^{3+} ions sit in octahedral (1/2 occupied) sites in the lattice. Eight tetrahedral sites are occupied by Mg^{2+} ions, and 16 octahedral sites are filled by Al^{3+} ions surrounded by 32 O^{2-} ions in a unit cell of the spinel. In consequence, spinel has 56 ions per unit cell (see details in Klein & Hurlbut 1993; Fabian et al. 2001).

Spinel can be found as a natural mineral and can also be syntheszed. Mg^{2+} and Al^{3+} ions are originally well ordered in natural spinel lattices; however, the spinel crystal undergoes disordering by annealing. Disordering of these cations is seen in both annealed and synthetic crystal spinels. The structural transition occurs at temperatures between 1023 and 1073 K due to the disordering (see details in Schmocker et al. 1972; Fabian et al. 2001). The melting point of spinel is 2408 K (Lide 1990).

Possible spinel formation pathways depend on temperature. At higher temperature, spinel grains may be formed via the reaction

$$\mathrm{Mg(gas)} + 2\mathrm{Al(gas)} + 4\mathrm{O(gas)} \longrightarrow \mathrm{MgAl_2O_4(solid)}.$$

As the temperature drops around 1758 K, Al is not able to remain in the gas phase together with three oxygens for every two atoms. Thus, it is conceivable that spinel forms via a chemical reaction with corundum at lower temperature (≈1500 K)

$$\mathrm{Mg(gas)} + \mathrm{O(gas)} + \mathrm{Al_2O_3(cry)} \longrightarrow \mathrm{MgAl_2O_4(cry)}$$

("cry" denotes crystalline)(Grossman & Larimer 1974).

In addition, spinel formation has been confirmed in shock induced experiments by making use of single crystals of corundum and periclase (MgO) (Potter & Ahrens 1994). They reported that a $MgAl_2O_4$ layer is formed at the boundary between these two crystals under particular conditions. Hence, it is also possible that spinel forms via a solid-solid reaction with some shock impacts

$$\mathrm{MgO(cry)} + \mathrm{Al_2O_3(cry)} \longrightarrow \mathrm{MgAl_2O_4(cry)}.$$

The fundamental (one photon) lattice vibrations of spinel generate bands between 12.5 and 33.3 μm (800-300 cm^{-1}) (Tropf & Thomas 1991).

Optical properties of $MgAl_2O_4$ have been investigated by e.g. Tropf & Thomas (1991), Chihara et al. (2000), and Fabian et al. (2001). Chihara et al. (2000) and Fabian et al. (2001) derived the optical constants of both natural and synthetic spinels from reflectance measurements.

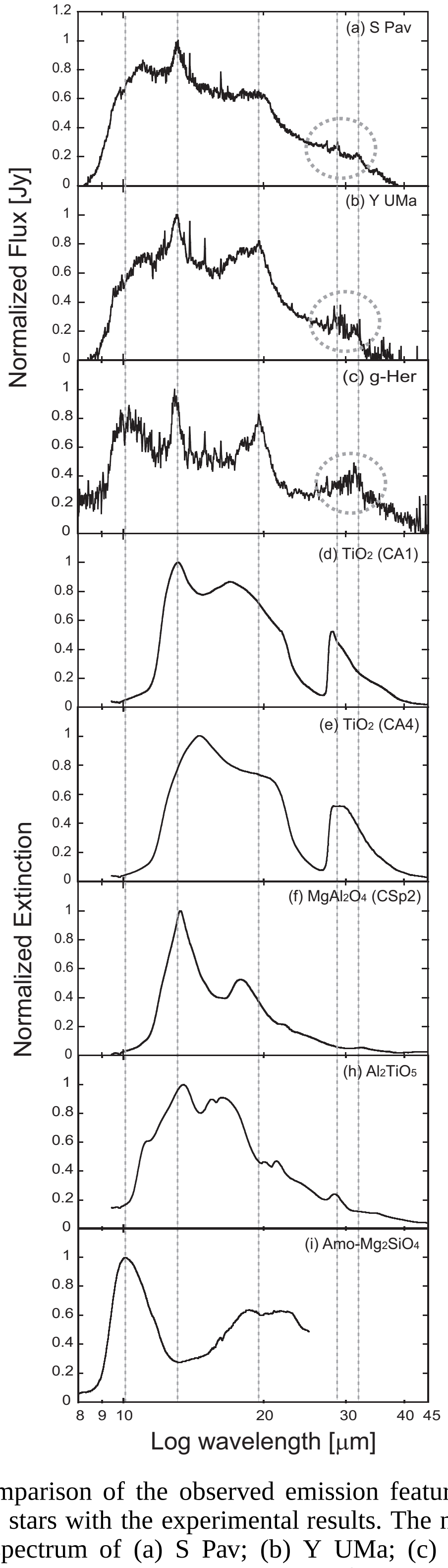

Fig. 8. Comparison of the observed emission features for the three AGB stars with the experimental results. The normalized emission spectrum of (a) S Pav; (b) Y UMa; (c) g Her are compared with the aerosol measurements of (d) anatase (CA1); (e) anatase (CA4); (f) spinel (CSp2); (g) tialite (Al_2TiO_5); (h) amorphous Mg_2SiO_4. The gray dotted lines denote 11, 13, 19.5, 28 and 32 μm wavelengths.